

This manuscript has not yet undergone peer-review. Subsequent versions of this manuscript may have slightly different content. If accepted, the final version of this manuscript will be available via the 'Peer-reviewed Publication DOI' link on the right-hand side of this webpage. Please feel free to contact the corresponding author.

1 High-resolution grids of daily air temperature for Peru 2 - the new PISCOt v1.2 dataset

3 Adrian Huerta^{1,2,*}, Cesar Aybar^{3,4}, Noemi Imfeld^{5,6}, Kris Correa¹, Oscar Felipe-Obando¹,
4 Pedro Rau⁷, Fabian Drenkhan⁸, and Waldo Lavado-Casimiro¹

5 ¹Servicio Nacional de Meteorología e Hidrología (SENAMHI), Lima, Perú.

6 ²Departamento de Física y Meteorología, Universidad Nacional Agraria La Molina (UNALM), Lima, Perú

7 ³Image Processing Laboratory, University of Valencia, 46980, Valencia, Spain

8 ⁴High Mountain Ecosystem Research Group, National University of San Marcos, 15081, Lima, Peru

9 ⁵Institute of Geography, University of Bern, Bern, Switzerland

10 ⁶Oeschger Centre for Climate Change Research, University of Bern, Bern, Switzerland

11 ⁷Centro de Investigación y Tecnología del Agua (CITA), Departamento de Ingeniería Ambiental, Universidad de
12 Ingeniería y Tecnología (UTECH), Lima, Perú

13 ⁸Geography and the Environment, Department of Humanities, Pontificia Universidad Católica del Perú, Lima, Peru

14 *corresponding author(s): Adrian Huerta (adrhuerta@gmail.com)

15 ABSTRACT

Gridded high-resolution climate datasets are increasingly important for a wide range of modelling applications. Here we present PISCOt (v1.2), a novel high spatial resolution (0.01°) dataset of daily air temperature for entire Peru (1981-2020). The dataset development involves four main steps: i) quality control; ii) gap-filling; iii) homogenisation of weather stations, and iv) spatial interpolation using additional data, a revised calculation sequence and an enhanced version control. This improved methodological framework enables capturing complex spatial variability of maximum and minimum air temperature at a more accurate scale compared to other existing datasets (e.g. PISCOt v1.1, ERA5-Land, TerraClimate, CHIRTS). PISCOt performs well with mean absolute errors of 1.4 °C and 1.2 °C for maximum and minimum air temperature, respectively. For the first time, PISCOt v1.2 adequately captures complex climatology at high spatiotemporal resolution and therefore provides a substantial improvement for numerous applications at local-regional level. This is particularly useful in view of data scarcity and urgently needed model-based decision making for climate change, water balance and ecosystem assessment studies in Peru.

17 Background & Summary

18 Air temperature is a fundamental parameter of the climate system, which is required for various applications
19 such as ecology¹, hydrology², public health³, agriculture⁴, climate variability, and climate change^{5,6}.
20 Typically, temperature values are obtained from meteorological stations and show high accuracy and
21 temporal resolution but do not capture information for an entire unit or region of analysis. Therefore,
22 gridded global- or continental-scale databases, derived from interpolated⁷, reanalyzed⁸ and/or combined⁹
23 in-situ and surface remote sensing data, are widely used. While each dataset offers several advantages
24 for specific applications, limitations related to complex topography, spatial resolution, and the amount of
25 assimilated data reduce their reliability^{10,11}. In recent years, gridded high-resolution climate datasets at
26 national and sub-national scales have been produced to close this gap¹²⁻¹⁸.

27 A broad range of methods exists for creating gridded air temperature data based on weather stations.
28 Traditionally, they have been divided into geostatistical, non-geostatistical, and combined methods^{19,20}.

29 Although these methods are widely used and provide high efficiency, more recent procedures based on
30 artificial intelligence including deep learning^{21,22} and machine learning^{23,24} are gaining relevance due to
31 their ability to work with large amounts of data and capture non-linear and multivariate relationships²⁵.
32 However, the reduced capacity to estimate the value outside the range of the training data limits its use
33 in large regions with low station density^{26,27}. Besides, since the relationship between air temperature
34 and auxiliary spatial predictors varies on spatiotemporal scales, recent research has also highlighted the
35 importance of non-stationarity in the spatiotemporal domain by building local models in contrast to global
36 estimation models^{13,28–32}. The diversity of methods has advantages and disadvantages regarding data
37 availability, computational efficiency, computational cost, and estimation accuracy. Therefore, the method
38 selected must be suitable or at least adapted to the purpose and study area.

39 In South America, only few efforts have been undertaken to create gridded temperature datasets, mainly
40 because of the low density of weather stations or the lack of long-term data series. However, there are
41 significant advances in the construction of gridded datasets in countries such as Brazil^{33,34}, Chile³⁵, and
42 Bolivia^{36,37}. For Peru, only two databases exist currently. The first is a gridded monthly-scale product for
43 1964–2014 at 5 km spatial resolution (henceforth "VS2018") developed by Vicente-Serrano³⁸. The second
44 is a gridded daily-scale product for 1981–2016 at 10 km developed by the National Service of Meteorology
45 and Hydrology (SENAMHI). SENAMHI introduced this product as part of the Peruvian interpolated
46 data of the Climatological and Hydrological Observations of SENAMHI (PISCO), denominated PISCOt
47 v1.1³⁹. Since its release, PISCOt has been applied in numerous areas of research and operation^{3,40–45}.
48 Due to the increasing availability of observed data and the need for higher spatial resolution, it is crucial
49 to account for gridded air temperature datasets that allow modelling and process understanding at local
50 scales, e.g., at the catchment level. Previously applied techniques^{46–49}, show that such a product can be
51 optimised by enhancing the temporal homogeneity of the observed data and also by using topographic and
52 climatic co-variables. Among the applied remote sensing data, Land Surface Temperature (LST) is the
53 most frequently used parameter because it improves both the numerical accuracy and the spatiotemporal
54 details of the interpolated air temperature.

55 Here, we present an updated version (v1.2) of PISCOt that consists of a gridded daily dataset for
56 maximum (Tmax) and minimum (Tmin) air temperature at a spatial resolution of 0.01° (≈ 1 km) for
57 the period 1981–2020. The updated version of PISCOt is essential for two main reasons: i) it provides
58 high-resolution estimates of daily Tmax and Tmin in a data scarce region taking into account steep climatic
59 gradients that occur over complex terrain; and ii) it provides the basis for further applications such as
60 studies related to climate change analysis, hydrological modelling, and ecology, among others.

61 **Methods**

62 **Workflow for generation of the data**

63 Missing, inhomogeneous, and non-quality-controlled data are a typical concern in hydro-climatological
64 studies. Particularly in regions with low financial resources and limited technical and institutional
65 capacities, weather station networks are often sparse with poor coverage in rural and remote areas, many
66 stations do not work appropriately, and quality control systems are inefficient^{50,51}. In Peru, quality issues
67 with station data are especially challenging due to the complex topography leading to steep climatic
68 gradients^{52,53}. The development of PISCOt requires therefore careful selection and pre-processing of the
69 station observations before spatial interpolation can be applied.

70 The selection of the horizontal resolution is crucial in the spatial interpolation process. From a
71 climatological perspective, deriving coarser products rather than topoclimatic-scale products¹³ (kilometer
72 or sub-kilometer) based on sparse interpolated observations does not yield additional information⁵⁴. The

73 underlying station distribution mostly defines the effective resolution, and it can be different from the target
74 grid spacing^{55–57}. However, from the user’s perspective, higher-resolution data can be more desirable
75 since they are urgently needed for practical applications⁵⁸. This is because these applications require a
76 clear characterization of local gradients which in complex terrain might occur over shorter distances. An
77 interpolation approach of air temperature based on high-resolution spatial predictors ($0.01^\circ \approx 1$ km) is
78 advantageous, especially in extremely complex mountain terrain such as the Andes, to properly account for
79 the orographic gradients in a wide range of applications. Additionally, using high-resolution data makes it
80 easier to interpret satellite observations or use them in hydrological models without further downscaling.

81 Therefore, the workflow for the development of the new PISCOt dataset includes four steps: i) quality
82 control, ii) gap-filling, iii) homogenisation of weather stations, and iv) spatial interpolation (Fig. 1). In
83 step i), statistical and visual techniques were applied to remove erroneous data in the times series of Tmax
84 and Tmin. For ii), all time series were gap-filled using data from neighbouring stations. The previously
85 gap-filled data were then homogenised in step iii) to reduce temporal inhomogeneities. Once a complete
86 and homogenised database of Tmax and Tmin observations was established, we proceeded to step iv). A
87 climatologically based interpolation approach^{59–62} was used, where the spatial interpolation was divided
88 into the mean monthly normal and anomalies, and then aggregated to obtain the final product. Topographic
89 and remote sensing data served as a basis to estimate air temperature at the country scale. The following
90 sections provide the data sources and four development steps in more detail.

91 **Weather station data**

92 ***Data source***

93 The database used in this study belongs to the Peruvian weather service SENAMHI and includes 430 daily
94 series of Tmax and Tmin (Fig. 2). To obtain a better spatial representation of the country boundaries (Fig.
95 2a), we used additional data from adjacent countries including the National Institute for Meteorology and
96 Hydrology (INAMHI), the Institute of Hydrology, Meteorology and Environmental Studies (IDEAM),
97 the National Institute of Meteorology (INMET), and the Explorador Climático portal from the Center for
98 Climate and Resilience Research (CR2). In total, 32 additional data series were obtained from Bolivia (3
99 time series), Brazil (5), Chile (3), Colombia (3), and Ecuador (18), leading to a total of 462 potential time
100 series for this study (Fig. 2b).

101 The spatial distribution of the stations is highly uneven in the study area. While in the Amazon region,
102 only a limited number of stations exists, station density in the Andes is higher and largest at the Pacific
103 Coast (Fig. 2). Depending on the altitude, there was a lower (higher) density of stations between 1000
104 and 2000 masl (0–1000 masl and > 3000 masl)⁶³. Thus, the spatial distance between stations varied
105 considerably. The earliest observations started in the 1930s, with a significant increase up to date. Due to
106 political instability and social conflicts (Supplementary Fig. 1), two episodes of under-reporting occurred
107 before 1960 and during the 1980s. Due to the low reliability of data before the 1980s, the gridded product
108 only covers the period 1981 to 2020. In addition, only stations with at least five years of data (365
109 days of the year repeated at least five times) were used. The 5-year threshold was chosen based on the
110 finding that at least 5-7 years of observations are required before pairwise relationships between stations
111 stabilise^{13,64,65}.

112 ***Quality control***

113 The quality control (QC) of the air temperature series comprised the following steps:

- 114 1. Obvious errors: conversion of numerical values (-999, -99.9, -88.8) to empty values, and removal of
115 duplicate or incorrectly formatted dates.

- 116 2. Extreme values: flagging of extreme (low and high) air temperature values based on physical and
117 statistical values. The physical maximum and minimum limits for Tmax (Tmin) were 60 °C and -10
118 °C (40 °C and -30 °C), respectively⁶⁶. The statistical algorithm identified records that are above
119 (below) the 3rd (1st) quartile plus or minus m times the interquartile range (IRQ). For Tmax and
120 Tmin, m was set to 3.5.
- 121 3. Internal consistency: inspection of records where Tmax is below Tmin. Also, values where flagged,
122 when Tmax and Tmin had the same magnitude (Tmax = Tmin).
- 123 4. Temporal coherence: inspection of values repeated over a long period and very extreme (day-to-day)
124 jumps. It was defined that a value can be the same up to a maximum of 8 days. In addition, a daily
125 jump may not have a variation over 20 °C⁶⁷.
- 126 5. Spatial coherence: comparison of the rank of each data value with the average rank of the data
127 recorded in adjacent stations⁶⁸. The original daily air temperature series were converted to per-
128 centiles. Each air temperature value was replaced by its corresponding percentile. For each time
129 series, we selected the neighbouring stations which meet the requirements of being within 70 km
130 and had an elevation difference of less than 500 m^{69,70}. For performing the test, at least four
131 neighbouring stations had to be available. If this was not the case, the daily value of the target
132 station was not compared. The records of the target station with differences greater than a percentile
133 of 0.85 concerning the average of the neighboring stations were identified. The percentile difference
134 approach allows for identifying only the most extreme spatial variations^{71–73}.
- 135 6. Visual inspection: a visual inspection of the time series was carried out to identify periods with inho-
136 mogeneities that cannot be corrected (rounding errors, asymmetric rounding patterns, measurement
137 precision, time irregularities, and obvious inhomogeneities)^{51,74}. For this purpose, we used daily
138 series and annual decimal frequency charts.

139 All QC-flagged values were set as a missing observation after the QC steps (Supplementary Fig. 1 and
140 2). For the following procedures, only stations that retained the 5-year threshold after the QC were used.
141 In addition, we manually verified the elevation information of weather stations using a digital elevation
142 model (detailed in the *Spatial predictors for air temperature* sub-section) and modified it where necessary.

143 **Gap-filling**

144 Simple interpolation of incomplete data may produce artificial inhomogeneities in the gridded product due
145 to the irregular spatiotemporal distribution of weather stations during the 1981–2020 period⁷⁵. This can
146 affect the variance and lead to erroneous conclusions on changes and variability⁷⁶. To reduce such artificial
147 inhomogeneities, data reconstruction of time series that do not cover the entire period and of gaps within
148 time series was necessary.

149 A gap-filling procedure based on neighbouring stations⁷⁷ was implemented to create a complete
150 database. Before applying the algorithm, the available information was standardised using a daily
151 climatology of the available data to avoid differences in the mean and the variance⁷⁸. Subsequently, the
152 model estimates were corrected to approximate the observed values as closely as possible. The correction
153 was made by applying empirical quantile mapping^{79,80}. The Tmax and Tmin series were reconstructed
154 independently.

155 A neighbouring station was considered for gap-filling if it met two conditions: (i) at least five years
156 of data in common, and (ii) a correlation greater than or equal to 0.6 with the target station. An iterative
157 process of the gap-filling algorithm was performed to take advantage of those stations that did not have a

158 common period at the beginning⁸¹. This was carried out in up to three iterations, where the availability of
159 neighbouring stations was limited according to the following characteristics: horizontal-vertical distances
160 of i) 70 km–500 m, (ii) 100 km–500 m, and (iii) 150 km (no vertical limit), respectively. A maximum of
161 8 neighbouring stations was considered during this procedure. The rationale for this configuration was
162 based on a previous correlation-distance-elevation analysis (Supplementary Fig. 3).

163 Due to the low density of weather stations in some regions, virtual stations (time series at the closest
164 grid point) from the ERA-5 Land reanalysis⁸² were additionally included to fill temporal gaps. These
165 time series were not directly used, but an anomaly-based bias correction (detrended empirical quantile
166 mapping⁸³) was applied to series with at least ten years of data. Only those virtual stations with a
167 correlation greater than or equal to 0.6 with the target station (within Peru) were preserved and used for
168 gap-filling.

169 **Homogenisation**

170 Many non-climatic influences can affect measurements (changes in station location, instrumentation,
171 and observing practices, among others). To eliminate these inhomogeneities and to obtain more reliable
172 observations, time series must be homogenised^{84,85}. A variety of statistical methods has been developed,
173 each with different results^{84,86}. In sparse networks, homogenisation performance is drastically reduced,
174 and there is a risk of erroneous corrections due to the low signal-to-noise ratio⁸⁷. Consequently, the chosen
175 method must be applied carefully.

176 We tested the temporal homogeneity using the Standard Normal Homogeneity Test^{88,89} in both its
177 relative form, known as the Pairwise Homogeneity Algorithm (PHA)^{90,91}, and its absolute implementation.
178 The process was fully automatic and straightforward. Therefore, the approach was consistent, unlike
179 semi-automatic approaches that require several subjective decisions that can influence the whole process⁷⁴.
180 In addition, PHA has been applied at global scale datasets^{92,93}, and is one of the approaches with the best
181 performance^{84,86}.

182 The algorithm searched a maximum (minimum) of eight (four) neighbouring reference stations with a
183 correlation greater than or equal to 0.6 with the target station within a horizontal (vertical) distance of
184 1000 km (1000 m) in order to perform a relative test. In absence of these conditions, the absolute test was
185 applied. Absolute tests have a lower detection efficiency than relative tests⁸⁴. Therefore, the condition was
186 designed as a backup test when a relative test was almost impossible to apply⁹⁴. In both cases, a p -value
187 < 0.05 (with a 95% confidence interval) was used to define significant breakpoints which were then used
188 to adjust past values compared to the present.

189 As the algorithm was applied on a monthly scale, a linear time interpolation of the monthly correction
190 factors to a daily scale was performed⁹⁵. The homogeneity tests were applied after the gap-filling to
191 i) detect inhomogeneities introduced by the gap-filling process, and, ii) because the process was more
192 reliable if the time series had no gaps^{50,71}. Finally, as for the gap-filling procedure, homogenisation was
193 performed in up to three repetitive cycles according to the boundary conditions previously defined.

194 **Spatial predictors for air temperature**

195 In the gridding process, Tmax and Tmin were adjusted to a series of auxiliary spatial predictors such
196 as land surface temperature (LST), elevation (DEM), latitude (Y), longitude (X), and the topographic
197 dissection index (TDI).

198 The LST observations were selected from MODIS⁹⁶. This satellite product provides average 8-day
199 values starting in the year 2000 and at a 1 km spatial resolution. The Terra version (MOD11A2 V6)⁹⁷ was
200 used for day (LST_day) and night (LST_night) observations. Because of missing data before 2000, the
201 average monthly values for 2000-2020 for both day and night times were used as spatial predictors for

202 Tmax and Tmin, respectively. Only LST values were used without cloud contamination, emissivity error >
203 0.02, or LST errors > 2 °C. If any pixels in the final average were empty, they were reconstructed through
204 nearest neighbour interpolation. The LST was downloaded from [https://developers.google.com/earth-
205 engine/datasets/catalog/MODIS_006_MOD11A2](https://developers.google.com/earth-engine/datasets/catalog/MODIS_006_MOD11A2) (accessed 31 October 2022).

206 The DEM data were obtained from the Global Multi-resolution Terrain Elevation Data (GMTED)
207 2010⁹⁸ at a spatial resolution of 1 km. This dataset was selected because it has also been used in other
208 temperature-gridded products at a national level³⁸. X, Y, and TDI were derived at the same spatial resolu-
209 tion as the DEM. The digital elevation model was downloaded from [https://developers.google.com/earth-
210 engine/datasets/catalog/USGS_GMTED2010](https://developers.google.com/earth-engine/datasets/catalog/USGS_GMTED2010) (accessed 31 October 2022).

211 The TDI was calculated through a multi-scale DEM calculation:

$$TDI_{(s_0)} = \sum_{i=1}^n \frac{Z(s_0) - Z_{min}(i)}{Z_{max}(i) - Z_{min}(i)} \quad (1)$$

212 Where $TDI_{(s_0)}$ is the final multi-scale TDI value for the grid cell location s_0 , $Z(s_0)$ is the elevation at
213 the grid cell location s_0 , $Z_{min}(i)$ is the minimum elevation at the grid cell location in the spatial window i ,
214 $Z_{max}(i)$ is the maximum elevation at the grid cell location in the spatial window i , and n is the number of
215 spatial windows⁹⁹. The TDI value for a specific window size represented the height of a grid cell relative
216 to the surrounding terrain. The multi-scale TDI was calculated for five spatial window sizes (at 3, 6, 9,
217 12, and 15 km). Valley bottoms and low areas relative to surrounding grids have values close to zero,
218 while ridges and areas above surrounding areas have high values approaching 5. The selection of this
219 topographic variable was based on the high correlation with daily Tmin anomalies which are influenced
220 by cold air drainage^{13,99}.

221 The spatial predictors were downloaded from the Earth Engine Data Catalog¹⁰⁰ repository via `gce`¹⁰¹.
222 For efficient processing, the data were adapted to the extent of -81.405°, -67.185°, -18.595°, and 1.225°
223 (min longitude, max longitude, min latitude, and max latitude); and re-gridded at 0.01° spatial resolution.

224 **Air temperature interpolation**

225 For the interpolation of Tmax and Tmin, a climatologically aided interpolation (CAI) approach^{59–62}
226 was used. With CAI, deviations from the average (anomalies) on a given day were interpolated and
227 combined with an average field (climatology) to produce the final daily product. The CAI approach has
228 been employed in several studies^{13,18,62,73} and has proven to be effective to improve the accuracy of air
229 temperature estimation in regions of complex terrain with limited observations^{102–105}. This approach
230 drastically reduced computational costs compared to independent runs for each time step, and the co-
231 variables did not necessarily need to be in the same temporal range as the observational data. The procedure
232 was applied independently for Tmax and Tmin and comprised three steps:

- 233 1. Interpolation at monthly (normal) average scale for the 1981-2010 period.
- 234 2. Interpolation at the daily anomaly scale (based on the monthly normal) for 1981–2020 period.
- 235 3. Combination of 1 and 2 to obtain the daily temperature value.

236 **Monthly normal interpolation**

237 For the interpolation of the monthly normal, the Regression-Kriging (RK) method^{13,29,106} was used,
238 which represents a spatial process expressed as the sum of a deterministic and a stochastic part:

$$\bar{T}(s_0, m_0) = \bar{T}_u(s_0, m_0) + \bar{T}_e(s_0, m_0) \quad (2)$$

239 Where $\bar{T}(s_0, m_0)$ is the final interpolated normal temperature at the grid cell location s_0 and for the
 240 month m_0 , $\bar{T}_u(s_0, m_0)$ is the deterministic spatial trend in normal temperature modelled by the weather
 241 station locations and auxiliary predictors, and $\bar{T}_e(s_0, m_0)$ is the spatially autocorrelated stochastic residual
 242 with zero mean¹⁰⁷. We use a linear model to fit $\bar{T}_u(s_0, m_0)$, and ordinary kriging (OK) to interpolate the
 243 residual part $\bar{T}_e(s_0, m_0)$:

$$\bar{T}(s_0, m_0) = \beta_0 + \beta_1 lst(m_0) + \beta_2 z + \beta_3 x + \beta_4 y + \sum_{i=1}^n w_i(s_0, m_0) \bar{T}_e(s_i, m_0) \quad (3)$$

244 β_0 is the intercept; β_1 , β_2 , β_3 and β_4 are the model coefficient estimates for monthly average LST,
 245 elevation, latitude, and longitude, respectively; $lst(m_0)$, z , x and y are the average LST at m_0 , elevation,
 246 longitude, and latitude at grid level at the location s_0 ; $w_i(s_0, m_0)$ are the weights defined by the residual
 247 spatial covariance; and $\bar{T}_e(s_i, m_0)$ are the residuals of the regression for n stations.

248 Due to the large variability and extent of the study area, it was not appropriate to use a global
 249 model for the spatial prediction of normal temperature. A version of RK with a moving spatial window
 250 based on Geographically Weighted Regression-Kriging (GWRK)¹⁰⁸ was used to account for the spatial
 251 heterogeneity in the interpolation process. The GWR^{109,110} calculated local trends for a subset of the
 252 study area with a weighting of weather stations using a distance-based function. To improve prediction
 253 accuracy, it added the OK from the residuals to the regression estimate. The weighting of the observations
 254 in GWR was calculated using the bi-square kernel nearest neighbourhood function:

$$w_i(s_0) = \left[1 - \left(\frac{h(s_0)_i}{r} \right)^2 \right]^2 \quad (4)$$

255 Where $w_i(s_0)$ is the distance-based weighting function of the station i at the interpolation location
 256 s_0 , $h(s_0)$ is the distance between the station i and the interpolation location s_0 , r is the bandwidth for
 257 the size of the spatially adaptive kernel function. The bandwidth optimisation was necessary because a
 258 significant deviation in estimating the regression parameters would be generated if the bandwidth were too
 259 large or too small¹⁰⁹. The Corrected Akaike Information Criterion automatically determined the optimal
 260 bandwidth¹¹⁰.

261 The regression coefficients of the GWR model were estimated at a spatial resolution of 0.1° , assuming
 262 that the relationship between the normal temperature and the auxiliary predictors is independent of the
 263 spatial resolution scale^{111,112}. Then it was locally interpolated with a bilinear approach at a resolution
 264 of 0.01° to be applied to the auxiliary predictors. The OK of the residuals was set to 0.05° and then
 265 disaggregated to 0.01° to reduce the measurement precision inconsistencies^{51,113,114} of the observed time
 266 series (Supplementary Fig. 4). Both sub-products at the final resolution were aggregated according to
 267 Equation 3 to obtain the grids of the monthly normals of Tmax and Tmin.

268 We used the GWmodel¹¹⁰ and gstat^{115,116} packages for the implementation of GWRK. For the
 269 estimation of the theoretical variogram (in OK), an automatic adjustment by iteratively repeated minimum
 270 squares was used, and the nugget value was forced to zero according to the automap package¹¹⁷.

271 **Daily interpolation**

272 A method similar to the monthly normal temperature was used in the daily temperature interpolation.
273 In this sense, the daily anomalies of Tmax and Tmin were expressed as the sum of two components
274 (deterministic and stochastic). Because of the large number of days (14244) per variable and the intention
275 to produce PISCOt operationally, it was chosen to use RK due to computational limitations. The model
276 here was similar to Equation 3 but added the spatial predictor TDI.

277 Therefore, the daily temperature product was obtained according to:

$$T(s_0, d_0) = \bar{T}(s_0, m_0) + \delta T(s_0, d_0) \quad (5)$$

278 Where $T(s_0, d_0)$ is the temperature at the interpolation point s_0 for the day d_0 within the month m_0 ,
279 $\bar{T}(s_0, m_0)$ is the normal temperature in the month m_0 according to Equation 3, and $\delta T(s_0, d_0)$ is the daily
280 temperature anomaly at the interpolation point s_0 for the day d_0 .

281 Unlike traditional CAI applications, we employed spatial predictors in $\bar{T}(s_0, m_0)$ and $\delta T(s_0, d_0)$ ^{13,39}.
282 Some research have found that topographic factors in a mountainous region are directly related to the spatial
283 patterns of $\delta T(s_0, d_0)$, particularly during stable atmospheric conditions that favour cold air inversion^{13,99}.

284 **Data Records**

285 The generated dataset consists of gridded, geo-localised files and a chart presenting information on the
286 weather stations used. For quick access, the data are divided into different repositories (Table 1) and are
287 stored in a figshare collection¹¹⁸ (<https://doi.org/10.6084/m9.figshare.c.5959863>).

288 The files of normal (average) and daily Tmax and Tmin values are stored in Repository 1 and 2,
289 respectively. These data represent the primary output of the research (a gridded 0.01° spatial resolution
290 product, PISCOt v1.2) and are available in the Network Common Data Form (NetCDF) format. Normal
291 values are stored in a single file whereas daily values are stored in different archives divided by year from
292 1981 to 2020.

293 The files of the spatial covariables are stored in Repository 3. These represent the predictors (X, Y,
294 DEM, LST_day, and LST_night) used to build the spatial models of Tmax and Tmin and are available in
295 NetCDF format.

296 The list of all weather stations used as input for PISCOt v1.2 is stored in Repository 4. The file contains
297 the following information (headers): code (*ID*), name (*NAM*), longitude (*LON*), latitude (*LAT*), elevation
298 (*ALT*), and source (*SRC*) of each weather station. In addition, it also provides information if a weather
299 station has been selected as a virtual station (bias-correction of ERA5-Land) in the gap-filling procedure
300 (*filter_qc*); and, if a weather station has been used for cross-validation in the gap-filling procedure and
301 daily spatial model (*filter_qc70*). The file is available in Comma Separated Values (CSV) format.

302 The gridded product of PISCOt v1.2 was also produced at a coarser spatial resolution (at 0.05° and
303 0.10°) using the same methodology and input data. This dataset is available in Repository 5. The purpose
304 to provide these different versions is to facilitate quick access to the data of Tmax and Tmin as the original
305 version (0.01°) includes large file sizes. The normal and daily values of Tmax and Tmin at 0.05° and
306 0.10° spatial resolution are stored in single NetCDF files.

307 The data in each NetCDF file consists of three dimensions (*time*, *latitude*, and *longitude*). For monthly
308 normal files, the *time* dimension corresponds to the month of the year beginning with January. Each
309 repository in Table 1 provides in addition a README file with a brief explanation of the dataset. Finally,
310 Repositories 1 and 2 will also be available as a secondary repository in the Google Earth Engine Data
311 Catalog.

312 **Technical Validation**

313 The development process of PISCOt has been evaluated in three steps: (i) gap-filling validation; (ii) spatial
314 model validation; and (iii) usefulness of the PISCOt product. In the spatial model validation, we focused
315 on the assessment at monthly normal and daily scales. In the usefulness of the PISCOt product, we
316 provided two applications, one associated with spatio-temporal variability of air temperature, and the other
317 related to the coastal fog effect on air temperature.

318 The statistics used to evaluate the skill of each step were simple error (mean bias), mean absolute error
319 (MAE), and the refined index of agreement (d_r)¹¹⁹. The d_r metric ranges from -1.0 to 1.0, with a value of
320 > 0.5 indicating a higher predictive capacity than the observed average. Because the primary mode of
321 variability in temperature is usually the seasonal cycle, the metrics were calculated independently for each
322 month and then averaged. This baseline adjustment in d_r prevented from overestimating the skill of each
323 reconstruction (i.e. gap-filling, etc.) by correcting for the seasonal cycle¹²⁰.

324 **Gap-filling validation**

325 A gap-filling procedure was applied to extend shorter times series of weather stations (back to 1981)
326 before constructing PISCOt. Two analyses were conducted to evaluate the efficiency of the gap-filling
327 procedure. (i) Validation: comparing infilled and observed data for available dates with observed values,
328 i.e., comparing available data that has been used to build the model. (ii) Cross-validation: comparing
329 infilled and observed data for dates that were artificially set as missing data, i.e., comparing data that has
330 not been used to build the model. In cross-validation, it is assumed a worst-case missing data scenario, we
331 set only ten years of data in stations with more observed data (in time series with $\geq 75\%$ of non-missing
332 data in the period 1981-2020).

333 Table 2 summarises the statistical metrics, and Figure 3 shows the distribution of d_r for both ex-
334 periments. The experiments showed that the efficiency was slightly better for Tmax than Tmin. Both
335 experiments had a bias < 0.2 °C and MAE < 1.5 °C. The most significant difference was in d_r ; although
336 moderate-to-high efficiency values were obtained in both experiments ($d_r > 0.5$), the best results were
337 obtained in experiment (i). This can be explained due to the small amount of information available in the
338 experiment (ii), as it was a worst-case scenario. By visualising the spatial distribution of d_r , it was noted
339 that there were higher (lower) values in more (less) dense regions of weather stations for both experiments.
340 The areas where d_r reached values from 0.8 to 0.9 were found in experiment (i). On the other hand, in
341 experiment (ii), it reached values from 0.6 to 0.7.

342 In general, the validation errors showed that the here-in used infill models worked reasonably well,
343 considering the complicated topographic variability of the study area and the limited observational data.
344 It must be pointed out that the errors of experiment (i) represented the residuals between the filled and
345 observed values, as these were used to construct the infilled models that were finally used in PISCOt.

346 **Spatial model validation**

347 ***Monthly normal air temperature***

348 K-fold cross-validation was performed to characterise the efficiency of the spatial model for the monthly
349 normal temperature. In this study, K = 10 was defined. Therefore, 10 clusters were set up for each model
350 and data series. We applied the statistical metrics (bias and MAE) at the scale of two seasonal periods:
351 "warm" (October to March) and "cold" (April to September).

352 Figure 4 showed a smaller positive bias in Tmax than in Tmin, with an average (warm and cold) value
353 of 0.15 °C and 0.25 °C, respectively. However, this may be biased due to negative errors in the average.
354 Considering the biases at the station scale, more points fall within the range of -1 °C to 1 °C in Tmin,
355 implying that the estimation was better for Tmin. This pattern confirmed the findings for MAE, where

356 Tmin (Tmax) averages 1.22 °C (1.42 °C) for both seasons. Spatially, the monthly normal interpolation
357 performed worst in the mountainous regions between the boundaries of the climatic regions (Pacific Coast
358 - Andes and Andes - Amazon), mainly in Tmax. Similarly, the largest errors in Tmax can be found in the
359 southern Pacific Coast. At the seasonal level, there was no considerable difference in Tmax. However, for
360 Tmin, estimates were slightly better in the warm period than in the cold period.

361 These results showed that the monthly normal interpolation for Tmin tends to be more efficient than for
362 Tmax. In order to understand the impact of the spatial predictors (LST and DEM) on the air temperature
363 estimation, the Lindemann, Merenda, and Gold method was applied^{13,121,122}. This method quantifies the
364 relative influence of a spatial covariate by partitioning the total variance explained by the R^2 of the model
365 (Figure 5).

366 In Tmax (Figure 5a), the DEM had the highest relative importance. The DEM contributed slightly
367 more in summer than in winter months. About 50% (40%) of the observed variance can be explained by
368 DEM in summer (winter). LST, on the other hand, adopts a major role from summer to autumn rather than
369 during the period from winter to spring. One probable reason why DEM was such a good predictor for
370 Tmax is that Tmax generally has a decreasing simple linear relationship with DEM, and DEM already
371 has a solid predictive capacity without the addition of LST^{13,28,47,123}. In addition, LST_day is highly
372 influenced by incoming solar radiation and biophysical properties (e.g. land cover, albedo, moisture,
373 roughness) and, thus, has a high degree of microscale variability¹²⁴. As a result, LST_day is more spatially
374 variable than Tmax, especially during higher solar radiation dates⁴⁷. The relationship between Tmax and
375 LST is often more complex than that between Tmin and LST^{13,47}. From a seasonal perspective, we found
376 that LST_day is more efficient in explaining the variance of Tmax from summer to autumn rather than
377 winter to spring. We hypothesize that this behaviour can be related to solar radiation seasonality which
378 is coupled with the cloud cover amount due to the rainfall season^{42,75}. From winter to spring (summer
379 to autumn) there is more (less) incoming solar radiation due to the presence of less (more) cloud cover.
380 Consequently, the spatial relation between LST_day and Tmax is weaker in the winter season compared
381 to the summer period.

382 For Tmin, LST was a slightly more critical predictor than DEM in most months except for February
383 (Figure 5b). However, no covariate reached a relative importance of 50%. It is somewhat notable that LST
384 reached its highest values from June to November and, inversely, in DEM. Due to the strong gradients
385 and complex topography, micro-climatic influences on Tmin play an essential role. Cold air inversions
386 are a common phenomenon, especially during periods of atmospheric stability and significant radiative
387 cooling which is typical for mountainous regions^{28,99}. Therefore, Tmin does not have a simple linear
388 relationship with DEM, which can limit its capacity as an individual predictor for the spatial patterns of
389 Tmin¹²⁵. The addition of LST, however, contributed to the spatial estimation of Tmin. Unlike LST_day,
390 without direct solar radiation LST_night spatial variability is more influenced by local and mesoscale
391 atmospheric processes important for air temperature¹²⁴. Therefore, LST_night and Tmin maintain similar
392 spatial variability throughout the annual seasonal cycle as contrary to LST_day and Tmax^{13,47,126}. This is
393 also shown by the fact that higher values of R^2 were reached with Tmin (Figure 5c) than with Tmax.

394 In summary, it was shown that the spatial model used had a greater predictive capacity and a lower
395 average error in the estimation of Tmin than Tmax, mainly during the summer months. LST had a higher
396 value-added in Tmin than in Tmax in the study region. Furthermore, DEM was more important for Tmax
397 prediction.

398 **Daily air temperature**

399 The evaluation of the efficiency of daily air temperature data was similar to the one presented for the
400 monthly normals, but only focused on the stations with long time series (with $\geq 75\%$ of non-missing data)

401 to reduce the influence of synthetic data.

402 Figure 6 shows the results for bias and MAE, while Figure 7 shows the results for d_r . On average, a
403 lower bias was observed compared to the normal scale. This was probably due to the greater amount of
404 averaged data. Despite this, it can be observed that there was a similar pattern to the normal scale. For the
405 bias (MAE), values of -0.01 °C and 0.05 °C (1.36 °C and 1.11 °C) were found on average for Tmax and
406 Tmin, respectively. Furthermore, estimates were slightly better for Tmax (Tmin) in the cold (warm) period.
407 d_r and reached moderate-to-high efficiency values ($d_r > 0.5$) at most of the weather stations. Efficiency
408 values were lowest for the warm period of Tmax ($d_r = 0.48$). The area with the lowest d_r values was in the
409 south, mainly along the Pacific Coast and the border regions of the Andes and the Amazon.

410 In addition, trends (Sen's slope estimator) were computed over the available period for each station
411 and were compared with trends calculated based on the 10-fold cross-validation. This analysis allows to
412 estimate how reliable temperature trends can be predicted at un-sampled locations by interpolation, giving
413 insight into the accuracy of temperature trends from the gridded dataset^{16,127}.

414 Figure 8 exhibits the cross-validated predictions of the 1981-2020 trends in the annual mean and the
415 warm and cold seasons of air temperature with the trends observed in the homogenized weather stations.
416 This shows that most signs of observed trends are well detected by the estimated time series, particularly
417 for Tmax rather than Tmin. The disparity is also evidenced by the d_r metric, where estimated trends for
418 Tmax are above 0.6 while for Tmin they are around 0.5 - 0.6. There is not much difference between
419 the annual and seasonal means. The results indicate that there is moderate efficiency in reproducing the
420 observed spatial variations of the temporal trend, there is a lower capability in Tmin rather than Tmax.
421 This is probably due to the limited station density in Peru and artificial temporal variability mixed with
422 real local climate features, despite the homogeneity check and QC procedures¹⁶. For the case of Tmin,
423 the lower temporal variability estimation can also be attributed to the temporal correlation power that
424 falls faster with distance compared to Tmax (Supplementary Figure 3), leading to a slightly less efficient
425 temporal reconstruction as shown in the *Gap-filling validation* sub-section.

426 In general, the results demonstrated a reasonably good capacity of the spatial model to estimate daily
427 Tmax and Tmin. Similarly to the results from the normal monthly scale, Tmin outperformed Tmax in both
428 the warm and cold periods. However, Tmax is slightly more efficient in estimating the observed spatial
429 variations of the temporal trend.

430 Usefulness of the PISCOt v1.2 product

431 *Spatio-temporal variability of air temperature*

432 To present an application of PISCOt v1.2, a description of the spatio-temporal variability of air temperature
433 indices characterising the trend (the non-parametric Mann-Kendall test and Sen's slope estimator) was
434 conducted. This was applied in the southern Andes of Peru, a region characterised by agricultural and
435 livestock subsistence and production⁴², and therefore highly dependent on climatic conditions. The indices
436 selected were annual mean Tmax (MTmax), annual mean Tmin (MTmin), and the annual number of frost
437 days (FD, number of days with Tmin < 0 °C).

438 Additionally, to provide a full comparison with existing temperature products, both national datasets
439 (PISCOt v1.1 and VS2018, described above) and global products (TerraClimate¹²⁸, CHIRTS⁹, and ERA5-
440 Land⁸²) were included. TerraClimate provides Tmax and Tmin at monthly temporal resolution and a ≈ 4
441 km spatial resolution for 1958–2020. CHIRTS produces daily values of Tmax and Tmin at 5 km (0.05°)
442 and is available from 1983 to 2016. ERA5-Land is a reanalysis product that contains a great diversity of
443 surface variables at a spatial resolution of 9 km ($\approx 0.1^\circ$) since 1981. For ERA5-Land, daily Tmax and
444 Tmin were obtained from the maximum and minimum hourly values.

445 First, the spatial differences for the annual average air temperature indices were examined for the

446 period 1981–2010. Figure 9a shows the annual climatologies of MTmax, MTmin, and FD in PISCOt
447 v1.2, while Figure 9b indicates the difference of PISCOt v1.2 with each gridded product. For MTmax,
448 differences were small (below 1 °C), mainly in PISCOt v1.1 and VS2018. ERA5-Land presented the
449 lowest MTmax values compared to PISCOt v1.2, reaching differences of up to more than 6 °C in large
450 parts of the Andean and Amazonian regions. The largest areas of differences between the multiple gridded
451 products occurred at the boundaries of the climatic regions, i.e., at the Andes-Amazon and Pacific-Andean
452 transitions and where no data were available. For MTmin, the spatial pattern of the differences was similar
453 to MTmax for PISCOt v1.1 and VS2018. The largest differences were found in TerraClimate and CHIRTS,
454 where the latter had the highest MTmin values, reaching differences of up to more than -6 °C in the
455 Andean highlands. For FD, PISCOt v1.1 and ERA5-Land showed the best agreement with PISCO v1.2
456 (differences within 10%). Only for CHIRTS, differences of up to 60% were discovered. This was not
457 surprising as CHIRTS represents the most diverging product regarding Tmin.

458 The spatio-temporal variability of air temperature indices was assessed through trend analysis at
459 different temporal and spatial windows. Figure 10 shows the decadal rate of change for 10-year time
460 windows from 1981 to 2020 for areas above 2000 masl in the Southern Andes of Peru. For MTmax, there
461 was a good agreement between the trends of the different products. Periods with significant positive trend
462 were coinciding well in all products in the 1990–1995, 2000–2005, and 2010–2015 years. Periods with
463 slightly negative or zero trends coinciding well in all products in the 1995–2000 and 2005–2010 years.
464 This was evident in PISCOt v1.2 compared to ERA5-Land, VS2018, and PISCOt v1.1. For MTmin, there
465 was more variability in the trends, with no clear overall direction as in MTmax, except for the latest years
466 (since 2010). From 1980 to 2000, PISCOt v1.2 showed similar variability (a slightly positive trend) to
467 ERA5-Land, then moves closer (a slightly negative trend) to PISCOt v1.1 and VS2018 in the 2000–2007
468 period, and finally, since 2010, being in agreement with PISCOt v1.1 and VS2018 and ERA5-Land
469 into a positive trend. It is worth noting that PISCOt v1.1 and VS2018 showed good agreement in Tmin
470 throughout the analysis period, diverging to a greater extent from PISCOt v1.2 before 1990. Significant
471 positive trends in common in MTmin were only found during 1990–1995 and 2010–2015. A similar pattern
472 as for MTmin was also found for FD. ERA5-Land (PISCOt v1.1) tended to behave analogously to PISCOt
473 v1.2 for much of the analysis period, only disagreement (agreement) from 1995 to 2007. There were only
474 significant overlapping trends in FD during 1990–1995 (negative) and 2010–2015 (positive).

475 Regarding spatial variability, Figure 11 shows the trend by different elevation intervals for the period
476 1983–2013 (common reporting period). In MTmax, the magnitude of trends increased for higher elevation
477 intervals mainly in PISCOt v1.2, PISCOt v1.1, VS2018, and ERA5-Land. In contrast, in CHIRTS and
478 TerraClimate no direct relationship between the elevation and trend magnitude was evident. There was
479 a more substantial spatial disparity in the direction of the trends at lower than high elevations in the
480 different products (Supplementary Fig. 5). For MTmin, the various products (except for CHIRTS) showed
481 a better agreement of the relationship between the trend magnitude and elevation. However, this was less
482 pronounced than for MTmax. Significant positive or negative trends in FD were only found between 3000
483 and 3500 masl, with a similar (inverse) agreement of PISCOt v1.2 with PISCOt v1.1 and ERA5-Land
484 (CHIRTS). PISCOt v1.2 and ERA5-Land reached zero trends above 5000 masl, because for this elevation
485 level for every year 100% FD was reached. Consequently, no temporal change can be found.

486 The results showed that PISCOt v1.2 performed well over the southern Andes of Peru. PISCOt v1.2
487 presented spatiotemporal trends and overall distribution similar to the other products. Some differences
488 in the results can be pointed out. Firstly, there was a high degree of correspondance in the magnitude of
489 the air temperature between PISCOt v1.2 and PISCOt v1.1 and VS2018. This was expected, since the
490 three datasets used information from the same station's network, albeit with a different number of stations
491 and distinct pre-processing applied. Larger differences were obtained in ERA5-Land (MTmax) and

492 CHIRTS (in MTmin and FD). ERA5-Land is a reanalysis-based dataset, thus, it is expected to represent
493 the physics. However, it was subject to systematic differences caused by the misrepresentation of the
494 topography, requiring a bias correction prior to its use at high elevations¹²⁹. CHIRTS is a merged product
495 of station-based and reanalysis data. In its construction, it prioritised the estimation of Tmax rather than
496 Tmin⁹, possibly explaining the significant differences with the latter variable. Considering the trends,
497 there was a clear warming signal^{5,38}, with larger magnitudes and spatially more homogeneously for Tmax
498 than for Tmin⁴². CHIRTS and TerraClimate showed largest differences in temporal and spatial trends,
499 leading to large unphysical trends due to unhomogenized or missing station data. This is an issue that
500 should be fixed by using homogenisation algorithms.

501 **Coastal fog effect on air temperature**

502 In order to assess PISCOt v1.2 at a daily time step, we provide an analysis of the effect of coastal fog
503 on modulating daily mean air temperature. Coastal fog frequently occurs at the Peruvian coast and
504 low Andean foothills. This phenomenon is especially persistent during austral winter (June-September),
505 although it can appear occasionally throughout the year¹³⁰⁻¹³². The occurrence of fog is often produced by
506 the particular thermal inversion layer situation with cool lower air masses due to the south-north flowing
507 Humboldt Current. The frequency of coastal fog increases gradually to the south, causing a marked diurnal
508 cooling in the affected coastal-Andean areas¹³².

509 We exemplified two situations of mean air temperature (Tmean: mean of Tmax and Tmin) during a
510 coastal fog-covered (2007/08/25) and cloud-free (2006/08/24) day in northern Peru including the Pacific
511 Coast and Andean slopes. These days were identified by Navarro-Serrano et al¹³² using the MODIS-Terra
512 satellite data. Figure 12 shows the spatial variability of Tmean during the two situations and its spatial
513 difference; in addition, the vertical distribution of Tmean with elevation was included for both days.
514 Tmean values are lower on the fog-covered day compared to the cloud-free day, reaching a contrast up to
515 2 - 6 °C. These higher Tmean differences reach approximately up to 500 masl which is close to the height
516 of the thermal inversion layer of 400 masl identified by Navarro-Serrano et al¹³². After that level, the
517 differences rapidly reduced and reached 0 °C. In addition, we found negative Tmean differences between
518 both situations above 2500 masl which can be also attributed to the presence of clouds at higher elevations
519 on the cloud-free day rather than on the fog-covered day. Interestingly, through a visual inspection of the
520 MODIS terra satellite images in Navarro-Serrano et al¹³² we noticed a higher amount of cloud cover at the
521 transition of the Andes-Amazon region during the cloud-free day, explaining the above-mentioned.

522 These results suggest that PISCOt v1.2 identified well the effect of coastal fog on air temperature.
523 Nevertheless, more in-depth analysis is required for a better understanding of this phenomenon.

524 **Usage Notes**

525 The PISCOt v1.2 database is a valuable dataset for different applications in Peru as it allows for high-
526 resolution analyses linked to e.g. climate change, health, hydrology, ecosystem assessments, and other
527 fields for research and practitioners. PISCOt v1.2 supports the generation of new findings urgently required
528 for more robust local decision-making in the scientific and political communities, especially in a context
529 of data scarcity and high uncertainties in the region.

530 The new PISCOt v1.2 product has improved compared to the earlier version 1.1 in several key aspects:
531 more assimilated time series, better consistency of station data pre-processing (quality control, gap-filling,
532 and homogenisation), use of updated freely available auxiliary predictors, higher spatial resolution, a tidier
533 and revised calculation sequence, and improved version control. Therefore, the development of PISCOt
534 v1.2 is more consistent, traceable, and reproducible compared to other previously established gridded
535 products in Peru.

536 PISCOt v1.2 adequately characterises the spatiotemporal variability of air temperature in average and
537 extreme values using indicators. However, within the scope of this study only three indices were used.
538 Future assessments therefore need to focus on more indicators of climate extremes not assessed in this
539 study.

540 As the region is topographically complex, including steep climatic gradients, and is characterized
541 by a low density and uneven distribution of weather stations, inherent limitations in spatial interpolation
542 are expected, mainly at high elevations (between 1000 and 2000 masl, and > 3500 masl). It is therefore
543 recommended to use PISCOt v1.2 along with other gridded multi-source products which would allow for
544 a better characterisation of the associated uncertainties in air temperature.

545 Furthermore, it is essential to clarify that matching weather stations with PISCOt v1.2 (and other
546 products) is not recommended for assessing air temperature accuracy¹³³. This is because such an analysis
547 would favour products with interpolation algorithms that constrain the gridded data to precisely match
548 weather station data. Likewise, if processes such as gap-filling, and homogeneity correction, among others,
549 are applied to the observed data before spatial interpolation, the updated information would therefore no
550 longer match the original data.

551 Finally, the gridded data of PISCOt v1.2 should only be used for continental areas. Due to the
552 differences in LST values over water bodies compared to their surrounding terrestrial landscapes and
553 the lack of observations over lakes, further validation is required to confirm the accuracy of spatial air
554 temperature patterns over water¹³. Estimates over e.g. water bodies should therefore be masked out (i.e.
555 be considered as empty grids).

556 Code availability

557 The construction of the gridded dataset PISCOt v1.2 was performed using the R (v3.6.3) and Python
558 (v3.8.5) programming languages. The entire code used is freely available at figshare and GitHub
559 (https://github.com/adrHuerta/PISCOt_v1-2) under the GNU General Public License v3.0.

560 References

- 561 1. Kessler, M., Toivonen, J. M., Sylvester, S. P., Kluge, J. & Hertel, D. Elevational patterns of *Polylepis*
562 tree height (Rosaceae) in the high Andes of Peru: role of human impact and climatic conditions.
563 *Front. plant science* **5**, 194, <https://doi.org/10.3389/fpls.2014.00194> (2014).
- 564 2. Rau, P. *et al.* Assessing multidecadal runoff (1970–2010) using regional hydrological modelling
565 under data and water scarcity conditions in Peruvian Pacific catchments. *Hydrol. Process.* **33**, 20–35,
566 <https://doi.org/10.1002/hyp.13318> (2019).
- 567 3. Delahoy, M. J. *et al.* Meteorological factors and childhood diarrhea in Peru, 2005–2015: a time
568 series analysis of historic associations, with implications for climate change. *Environ. Heal.* **20**,
569 1–10, <https://doi.org/10.1186/s12940-021-00703-4> (2021).
- 570 4. Sanabria, J., Calanca, P., Alarcón, C. & Canchari, G. Potential impacts of early twenty-first century
571 changes in temperature and precipitation on rainfed annual crops in the Central Andes of Peru. *Reg.*
572 *Environ. Chang.* **14**, 1533–1548, <https://doi.org/10.1007/s10113-014-0595-y> (2014).
- 573 5. López-Moreno, J. I. *et al.* Recent temperature variability and change in the Altiplano of Bolivia and
574 Peru. *Int. J. Climatol.* **36**, 1773–1796, <https://doi.org/10.1002/joc.4459> (2016).

- 575 6. Sulca, J. *et al.* Climatology of extreme cold events in the central Peruvian Andes during austral
576 summer: origin, types and teleconnections. *Q. J. Royal Meteorol. Soc.* <https://doi.org/10.1002/qj.3398>
577 (2018).
- 578 7. Harris, I., Osborn, T. J., Jones, P. & Lister, D. Version 4 of the CRU TS monthly high-resolution
579 gridded multivariate climate dataset. *Sci. data* **7**, 1–18, <https://doi.org/10.1038/s41597-020-0453-3>
580 (2020).
- 581 8. Hersbach, H. *et al.* The ERA5 global reanalysis. *Q. J. Royal Meteorol. Soc.* **146**, 1999–2049,
582 <https://doi.org/10.1002/qj.3803> (2020).
- 583 9. Verdin, A. *et al.* Development and validation of the CHIRTS-daily quasi-global high-resolution daily
584 temperature data set. *Sci. Data* **7**, 1–14, <https://doi.org/10.1038/s41597-020-00643-7> (2020).
- 585 10. Dee, D. P. *et al.* The ERA-Interim reanalysis: Configuration and performance of the data assimilation
586 system. *Q. J. Royal Meteorol. Soc.* **137**, 553–597, <https://doi.org/10.1002/qj.828> (2011).
- 587 11. Rao, Y., Liang, S. & Yu, Y. Land Surface Air Temperature Data Are Considerably Different Among
588 BEST-LAND, CRU-TEM4v, NASA-GISS, and NOAA-NCEI. *J. Geophys. Res. Atmospheres* **123**,
589 5881–5900, <https://doi.org/10.1029/2018JD028355> (2018).
- 590 12. Krähenmann, S. & Ahrens, B. Spatial gridding of daily maximum and minimum 2 m temperatures
591 supported by satellite observations. *Meteorol. Atmospheric Phys.* **120**, 87–105, <https://doi.org/10.1007/s00703-013-0237-9>
592 (2013).
- 593 13. Oyler, J. W., Ballantyne, A., Jencso, K., Sweet, M. & Running, S. W. Creating a topoclimatic daily air
594 temperature dataset for the conterminous United States using homogenized station data and remotely
595 sensed land skin temperature. *Int. J. Climatol.* **35**, 2258–2279, <https://doi.org/10.1002/joc.4127>
596 (2015).
- 597 14. Hiebl, J. & Frei, C. Daily temperature grids for Austria since 1961—concept, creation and applica-
598 bility. *Theor. Appl. Climatol.* **124**, 161–178, <https://doi.org/10.1007/s00704-015-1411-4> (2016).
- 599 15. Berezowski, T. *et al.* CPLFD-GDPT5: High-resolution gridded daily precipitation and temperature
600 data set for two largest Polish river basins. *Earth Syst. Sci. Data* **8**, 127–139, [https://doi.org/10.5194/](https://doi.org/10.5194/essd-8-127-2016)
601 [essd-8-127-2016](https://doi.org/10.5194/essd-8-127-2016) (2016).
- 602 16. Antolini, G. *et al.* A daily high-resolution gridded climatic data set for Emilia-Romagna, Italy,
603 during 1961–2010. *Int. J. Climatol.* **36**, 1970–1986, <https://doi.org/10.1002/joc.4473> (2016).
- 604 17. Way, R. G., Lewkowicz, A. G. & Bonnaventure, P. P. Development of moderate-resolution gridded
605 monthly air temperature and degree-day maps for the Labrador-Ungava region of northern Canada.
606 *Int. J. Climatol.* **37**, 493–508, <https://doi.org/10.1002/joc.4721> (2017).
- 607 18. Fonseca, A. R. & Santos, J. A. High-resolution temperature datasets in Portugal from a geostatistical
608 approach: Variability and extremes. *J. Appl. Meteorol. Climatol.* **57**, 627–644, <https://doi.org/10.1175/JAMC-D-17-0215.1>
609 (2018).
- 610 19. Li, J. & Heap, A. D. A review of comparative studies of spatial interpolation methods in en-
611 vironmental sciences: Performance and impact factors. *Ecol. Informatics* **6**, 228–241, <https://doi.org/10.1016/j.ecoinf.2010.12.003>
612 (2011). 1010.1236.
- 613 20. Li, J. & Heap, A. D. Spatial interpolation methods applied in the environmental sciences: A review.
614 *Environ. Model. Softw.* **53**, 173–189, <https://doi.org/10.1016/j.envsoft.2013.12.008> (2014).

- 615 **21.** Shen, H. *et al.* Deep learning-based air temperature mapping by fusing remote sensing, station,
616 simulation and socioeconomic data. *Remote. Sens. Environ.* **240**, 111692, <https://doi.org/10.1016/j.rse.2020.111692> (2020).
- 618 **22.** Zhang, X. *et al.* Deep learning-based 500 m spatio-temporally continuous air temperature generation
619 by fusing multi-source data. *Remote. Sens.* **14**, 3536, <https://doi.org/10.3390/rs14153536> (2022).
- 620 **23.** Sekulić, A., Kilibarda, M., Protić, D. & Bajat, B. A high-resolution daily gridded meteorological
621 dataset for Serbia made by Random Forest Spatial Interpolation. *Sci. Data* **8**, 1–12, <https://doi.org/10.1038/s41597-021-00901-2> (2021).
- 623 **24.** He, Q., Wang, M., Liu, K., Li, K. & Jiang, Z. GPRChinaTemp1km: a high-resolution monthly air
624 temperature data set for China (1951–2020) based on machine learning. *Earth Syst. Sci. Data* **14**,
625 3273–3292, <https://doi.org/10.5194/essd-14-3273-2022> (2022).
- 626 **25.** Lary, D. J., Alavi, A. H., Gandomi, A. H. & Walker, A. L. Machine learning in geosciences and
627 remote sensing. *Geosci. Front.* **7**, 3–10, <https://doi.org/10.1016/j.gsf.2015.07.003> (2016).
- 628 **26.** Hengl, T., Nussbaum, M., Wright, M. N., Heuvelink, G. B. & Gräler, B. Random forest as a
629 generic framework for predictive modeling of spatial and spatio-temporal variables. *PeerJ* **6**, e5518,
630 <https://doi.org/10.7717/peerj.5518> (2018).
- 631 **27.** Hernanz, A., García-Valero, J. A., Domínguez, M. & Rodríguez-Camino, E. A critical view on the
632 suitability of machine learning techniques to downscale climate change projections: Illustration for
633 temperature with a toy experiment. *Atmospheric Sci. Lett.* e1087, <https://doi.org/10.1002/asl.1087>
634 (2022).
- 635 **28.** Daly, C. *et al.* Physiographically sensitive mapping of climatological temperature and precipitation
636 across the conterminous United States. *Int. J. Climatol.* **28**, 2031–2064, <https://doi.org/10.1002/joc.1688>
637 (2008).
- 638 **29.** Hengl, T., Heuvelink, G. B., Tadić, M. P. & Pebesma, E. J. Spatio-temporal prediction of daily
639 temperatures using time-series of MODIS LST images. *Theor. Appl. Climatol.* **107**, 265–277,
640 <https://doi.org/10.1007/s00704-011-0464-2> (2012).
- 641 **30.** Lin, G. *et al.* Spatio-temporal variation of PM_{2.5} concentrations and their relationship with ge-
642 ographic and socioeconomic factors in China. *Int. J. Environ. Res. Public Heal.* **11**, 173–186,
643 <https://doi.org/10.3390/ijerph110100173> (2013).
- 644 **31.** Kilibarda, M. *et al.* Spatio-temporal interpolation of daily temperatures for global land areas at 1 km
645 resolution. *J. Geophys. Res.* **119**, 2294–2313, <https://doi.org/10.1002/2013JD020803> (2014).
- 646 **32.** Wang, M. *et al.* Comparison of spatial interpolation and regression analysis models for an estimation
647 of monthly near surface air temperature in China. *Remote. Sens.* **9**, <https://doi.org/10.3390/rs9121278>
648 (2017).
- 649 **33.** Xavier, A. C., King, C. W. & Scanlon, B. R. Daily gridded meteorological variables in Brazil
650 (1980–2013). *Int. J. Climatol.* **36**, 2644–2659, <https://doi.org/10.1002/joc.4518> (2016).
- 651 **34.** Xavier, A. C., Scanlon, B. R., King, C. W. & Alves, A. I. New Improved Brazilian Daily Weather
652 Gridded Data (1961–2020). *Int. J. Climatol.* <https://doi.org/10.1002/joc.7731> (2022).
- 653 **35.** Bianchi, E., Villalba, R., Viale, M., Couvreur, F. & Marticorena, R. New precipitation and
654 temperature grids for northern Patagonia: Advances in relation to global climate grids. *J. Meteorol.*
655 *Res.* **30**, 38–52, <https://doi.org/10.1007/s13351-015-5058-y> (2016).

- 656 **36.** Vicente-Serrano, S. M. *et al.* Average monthly and annual climate maps for Bolivia. *J. Maps* **12**,
657 295–310, <https://doi.org/10.1080/17445647.2015.1014940> (2016).
- 658 **37.** Andrade, M. F. *et al.* Atlas-clima y eventos extremos del altiplano central Perú-boliviano. *Geogr.*
659 *Bernensia* <https://doi.org/10.4480/GB2018.N01> (2018).
- 660 **38.** Vicente-Serrano, S. M. *et al.* Recent changes in monthly surface air temperature over Peru,
661 1964–2014. *Int. J. Climatol.* **38**, 283–306, <https://doi.org/10.1002/joc.5176> (2018).
- 662 **39.** Huerta, A., Aybar, C. & Lavado-Casimiro, W. PISCO temperatura versión 1.1 (PISCOt v1. 1). *Lima,*
663 *Peru: Natl. Meteorol. Hydrol. Serv. Peru (SENAMHI)* [https://iridl.ldeo.columbia.edu/SOURCES/](https://iridl.ldeo.columbia.edu/SOURCES/.SENAMHI/HSR/PISCO/Temp/)
664 [.SENAMHI/HSR/PISCO/Temp/](https://iridl.ldeo.columbia.edu/SOURCES/.SENAMHI/HSR/PISCO/Temp/) (2018).
- 665 **40.** Drenkhan, F., Huggel, C., Guardamino, L. & Haerberli, W. Managing risks and future options from
666 new lakes in the deglaciating Andes of Peru: The example of the Vilcanota-Urubamba basin. *Sci.*
667 *Total. Environ.* **665**, 465–483, <https://doi.org/10.1016/j.scitotenv.2019.02.070> (2019).
- 668 **41.** Muñoz, R., Huggel, C., Drenkhan, F., Vis, M. & Viviroli, D. Comparing model complexity for
669 glacio-hydrological simulation in the data-scarce Peruvian Andes. *J. Hydrol. Reg. Stud.* **37**, 100932,
670 <https://doi.org/10.1016/j.ejrh.2021.100932> (2021).
- 671 **42.** Imfeld, N. *et al.* A combined view on precipitation and temperature climatology and trends in the
672 southern Andes of Peru. *Int. J. Climatol.* **41**, 679–698, <https://doi.org/10.1002/joc.6645> (2021).
- 673 **43.** Llauca, H., Lavado-Casimiro, W., Montesinos, C., Santini, W. & Rau, P. PISCO_HyM_GR2M: A
674 Model of Monthly Water Balance in Peru (1981–2020). *Water* **13**, 1048, [https://doi.org/10.3390/](https://doi.org/10.3390/w13081048)
675 [w13081048](https://doi.org/10.3390/w13081048) (2021).
- 676 **44.** Monge-Salazar, M. J. *et al.* Ecohydrology and ecosystem services of a natural and an artificial
677 bofedal wetland in the central Andes. *Sci. The Total. Environ.* 155968, [https://doi.org/10.1016/j.](https://doi.org/10.1016/j.scitotenv.2022.155968)
678 [scitotenv.2022.155968](https://doi.org/10.1016/j.scitotenv.2022.155968) (2022).
- 679 **45.** Motschmann, A. *et al.* Current and future water balance for coupled human-natural systems—Insights
680 from a glacierized catchment in Peru. *J. Hydrol. Reg. Stud.* **41**, 101063, [https://doi.org/10.1016/j.](https://doi.org/10.1016/j.ejrh.2022.101063)
681 [ejrh.2022.101063](https://doi.org/10.1016/j.ejrh.2022.101063) (2022).
- 682 **46.** Chen, F., Liu, Y., Liu, Q. & Qin, F. A statistical method based on remote sensing for the estimation of
683 air temperature in China. *Int. J. Climatol.* **35**, 2131–2143, <https://doi.org/10.1002/joc.4113> (2015).
- 684 **47.** Oyler, J. W., Dobrowski, S. Z., Holden, Z. A. & Running, S. W. Remotely sensed land skin
685 temperature as a spatial predictor of air temperature across the conterminous United States. *J. Appl.*
686 *Meteorol. Climatol.* **55**, 1441–1457, <https://doi.org/10.1175/JAMC-D-15-0276.1> (2016).
- 687 **48.** Kloog, I. *et al.* Modelling spatio-temporally resolved air temperature across the complex geo-climate
688 area of France using satellite-derived land surface temperature data. *Int. J. Climatol.* **37**, 296–304,
689 <https://doi.org/10.1002/joc.4705> (2017).
- 690 **49.** Li, X., Zhou, Y., Asrar, G. R. & Zhu, Z. Developing a 1 km resolution daily air temperature dataset
691 for urban and surrounding areas in the conterminous United States. *Remote. Sens. Environ.* **215**,
692 74–84, <https://doi.org/10.1016/j.rse.2018.05.034> (2018).
- 693 **50.** Woldesenbet, T. A., Elagib, N. A., Ribbe, L. & Heinrich, J. Gap filling and homogenization of
694 climatological datasets in the headwater region of the Upper Blue Nile Basin, Ethiopia. *Int. J.*
695 *Climatol.* **37**, 2122–2140, <https://doi.org/10.1002/joc.4839> (2017).

- 696 **51.** Hunziker, S. *et al.* Identifying, attributing, and overcoming common data quality issues of manned
697 station observations. *Int. J. Climatol.* **37**, 4131–4145, <https://doi.org/10.1002/joc.5037> (2017).
- 698 **52.** Huerta, A. & Lavado-Casimiro, W. Atlas de Zonas Áridas del Perú: una evaluación presente y futura.
699 *Serv. Nac. de Meteorol. e Hidrología del Perú* <https://hdl.handle.net/20.500.12542/1206> (2021).
- 700 **53.** Zevallos, J. & Lavado-Casimiro, W. Climate Change Impact on Peruvian Biomes. *Forests* **13**, 238,
701 <https://doi.org/10.3390/f13020238> (2022).
- 702 **54.** Haylock, M. *et al.* A European daily high-resolution gridded data set of surface temperature
703 and precipitation for 1950–2006. *J. Geophys. Res. Atmospheres* **113**, [https://doi.org/10.1029/](https://doi.org/10.1029/2008JD010201)
704 [2008JD010201](https://doi.org/10.1029/2008JD010201) (2008).
- 705 **55.** Grasso, L. D. The differentiation between grid spacing and resolution and their application to
706 numerical modeling. *Bull. Am. Meteorol. Soc.* **81**, 579–580, [https://doi.org/10.1175/1520-0477\(2001\)](https://doi.org/10.1175/1520-0477(2001)082<0699:FCOTDB>2.3.CO;2)
707 [082<0699:FCOTDB>2.3.CO;2](https://doi.org/10.1175/1520-0477(2001)082<0699:FCOTDB>2.3.CO;2) (2000).
- 708 **56.** Lussana, C., Tveito, O. E., Dobler, A. & Tunheim, K. seNorge_2018, daily precipitation, and
709 temperature datasets over Norway. *Earth Syst. Sci. Data* **11**, 1531–1551, [https://doi.org/10.5194/](https://doi.org/10.5194/essd-11-1531-2019)
710 [essd-11-1531-2019](https://doi.org/10.5194/essd-11-1531-2019) (2019).
- 711 **57.** Crespi, A., Matiu, M., Bertoldi, G., Petitta, M. & Zebisch, M. A high-resolution gridded dataset of
712 daily temperature and precipitation records (1980–2018) for Trentino-South Tyrol (north-eastern
713 Italian Alps). *Earth Syst. Sci. Data* **13**, 2801–2818, <https://doi.org/10.5194/essd-13-2801-2021>
714 (2021).
- 715 **58.** Beven, K., Cloke, H., Pappenberger, F., Lamb, R. & Hunter, N. Hyperresolution information and
716 hyperresolution ignorance in modelling the hydrology of the land surface. *Sci. China Earth Sci.* **58**,
717 25–35, <https://doi.org/10.1007/s11430-014-5003-4> (2015).
- 718 **59.** Dawdy, D. & Langbein, W. Mapping mean areal precipitation. *Hydrol. Sci. J.* **5**, 16–23, <https://doi.org/10.1080/02626666009493176>
719 (1960).
- 720 **60.** Willmott, C. J. & Robeson, S. M. Climatologically aided interpolation (CAI) of terrestrial air
721 temperature. *Int. J. Climatol.* **15**, 221–229, <https://doi.org/10.1002/joc.3370150207> (1995).
- 722 **61.** New, M., Hulme, M. & Jones, P. Representing twentieth-century space–time climate variability. Part
723 II: Development of 1901–96 monthly grids of terrestrial surface climate. *J. climate* **13**, 2217–2238,
724 [https://doi.org/10.1175/1520-0442\(2000\)013<2217:RTCSTC>2.0.CO;2](https://doi.org/10.1175/1520-0442(2000)013<2217:RTCSTC>2.0.CO;2) (2000).
- 725 **62.** Hunter, R. D. & Meentemeyer, R. K. Climatologically aided mapping of daily precipitation and
726 temperature. *J. Appl. Meteorol.* **44**, 1501–1510, <https://doi.org/10.1175/JAM2295.1> (2005).
- 727 **63.** Condom, T. *et al.* Climatological and hydrological observations for the South American Andes: in
728 situ stations, satellite, and reanalysis data sets. *Front. Earth Sci.* **8**, 92, [https://doi.org/10.3389/feart.](https://doi.org/10.3389/feart.2020.00092)
729 [2020.00092](https://doi.org/10.3389/feart.2020.00092) (2020).
- 730 **64.** Hubbard, K. Spatial variability of daily weather variables in the high plains of the USA. *Agric. For.*
731 *Meteorol.* **68**, 29–41, [https://doi.org/10.1016/0168-1923\(94\)90067-1](https://doi.org/10.1016/0168-1923(94)90067-1) (1994).
- 732 **65.** Camargo, M. B. & Hubbard, K. G. Spatial and temporal variability of daily weather variables
733 in sub-humid and semi-arid areas of the United States high plains. *Agric. forest meteorology* **93**,
734 141–148, [https://doi.org/10.1016/S0168-1923\(98\)00122-1](https://doi.org/10.1016/S0168-1923(98)00122-1) (1999).
- 735 **66.** Vera, L., Villegas, E., Oria, C. & Arboleda, F. Control de calidad de datos de estaciones mete-
736 orológicas e hidrológicas automáticas en el centro de procesamiento de datos del SENAMHI.

- 737 Tech. Rep., Servicio Nacional de Meteorología e Hidrología del Perú (SENAMHI) (2021).
738 <https://www.senamhi.gob.pe/load/file/00711SENA-54.pdf>.
- 739 **67.** Espinoza, J. C. *et al.* Revisiting wintertime cold air intrusions at the east of the Andes: propagating
740 features from subtropical Argentina to Peruvian Amazon and relationship with large-scale circulation
741 patterns. *Clim. dynamics* **41**, 1983–2002, <https://doi.org/10.1007/s00382-012-1639-y> (2013).
- 742 **68.** Vicente-Serrano, S. M., Beguería, S., López-Moreno, J. I., García-Vera, M. A. & Stepanek, P.
743 A complete daily precipitation database for northeast Spain: reconstruction, quality control, and
744 homogeneity. *Int. J. Climatol.* **30**, 1146–1163, <https://doi.org/10.1002/joc.1850> (2010).
- 745 **69.** Lanzante, J. R. Resistant, robust and non-parametric techniques for the analysis of climate data:
746 Theory and examples, including applications to historical radiosonde station data. *Int. J. Climatol.*
747 *A J. Royal Meteorol. Soc.* **16**, 1197–1226, [https://doi.org/10.1002/\(SICI\)1097-0088\(199611\)16:](https://doi.org/10.1002/(SICI)1097-0088(199611)16:11<1197::AID-JOC89>3.0.CO;2-L)
748 [11<1197::AID-JOC89>3.0.CO;2-L](https://doi.org/10.1002/(SICI)1097-0088(199611)16:11<1197::AID-JOC89>3.0.CO;2-L) (1996).
- 749 **70.** Wood, W. H., Marshall, S. J., Whitehead, T. L. & Fargey, S. E. Daily temperature records from a
750 mesonet in the foothills of the Canadian Rocky Mountains, 2005–2010. *Earth Syst. Sci. Data* **10**,
751 595–607, <https://doi.org/10.5194/essd-10-595-2018> (2018).
- 752 **71.** Tomas-Burguera, M., Vicente-Serrano, S. M., Beguería, S., Reig, F. & Latorre, B. Reference
753 crop evapotranspiration database in Spain (1961–2014). *Earth Syst. Sci. Data* **11**, 1917–1930,
754 <https://doi.org/10.5194/essd-11-1917-2019> (2019).
- 755 **72.** Huerta, A. & Lavado-Casimiro, W. Trends and variability of precipitation extremes in the Peruvian
756 Altiplano (1971–2013). *Int. J. Climatol.* **41**, 513–528, <https://doi.org/10.1002/joc.6635> (2021).
- 757 **73.** Huerta, A. *et al.* PISCOeo_pm, a reference evapotranspiration gridded database based on FAO
758 Penman-Monteith in Peru. *Sci. data* **9**, 1–18, <https://doi.org/10.1038/s41597-022-01373-8> (2022).
- 759 **74.** Hunziker, S. *et al.* Effects of undetected data quality issues on climatological analyses. *Clim. Past*
760 **14**, 1–20, <https://doi.org/10.5194/cp-14-1-2018> (2018).
- 761 **75.** Aybar, C. *et al.* Construction of a high-resolution gridded rainfall dataset for Peru from 1981 to the
762 present day. *Hydrol. Sci. J.* **65**, 770–785, <https://doi.org/10.1080/02626667.2019.1649411> (2020).
- 763 **76.** Beguería, S., Vicente-Serrano, S. M., Tomás-Burguera, M. & Maneta, M. Bias in the variance
764 of gridded data sets leads to misleading conclusions about changes in climate variability. *Int. J.*
765 *Climatol.* **36**, 3413–3422, <https://doi.org/10.1002/joc.4561> (2016).
- 766 **77.** Thevakaran, A. & Sonnadara, D. U. Estimating missing daily temperature extremes in Jaffna, Sri
767 Lanka. *Theor. Appl. Climatol.* **132**, 145–152, <https://doi.org/10.1007/s00704-017-2082-0> (2018).
- 768 **78.** Beguería, S. *et al.* Gap filling of monthly temperature data and its effect on climatic variability and
769 trends. *J. Clim.* **32**, 7797–7821, <https://doi.org/10.1175/JCLI-D-19-0244.1> (2019).
- 770 **79.** Gudmundsson, L., Bremnes, J. B., Haugen, J. E. & Engen-Skaugen, T. Downscaling RCM precipita-
771 tion to the station scale using statistical transformations—a comparison of methods. *Hydrol. Earth*
772 *Syst. Sci.* **16**, 3383–3390, <https://doi.org/10.5194/hess-16-3383-2012> (2012).
- 773 **80.** Stanley, T., Kirschbaum, D. B., Huffman, G. J. & Adler, R. F. Approximating long-term statistics
774 early in the global precipitation measurement era. *Earth Interactions* **21**, 1–10, [https://doi.org/10.](https://doi.org/10.1175/EI-D-16-0025.1)
775 [1175/EI-D-16-0025.1](https://doi.org/10.1175/EI-D-16-0025.1) (2017).

- 776 **81.** Gonzalez-Hidalgo, J. C., Peña-Angulo, D., Brunetti, M. & Cortesi, N. MOTEDAS: a new monthly
777 temperature database for mainland Spain and the trend in temperature (1951–2010). *Int. J. Climatol.*
778 **35**, 4444–4463, <https://doi.org/10.1002/joc.4298> (2015).
- 779 **82.** Muñoz-Sabater, J. *et al.* ERA5-Land: A state-of-the-art global reanalysis dataset for land applications.
780 *Earth Syst. Sci. Data Discuss.* 1–50, <https://doi.org/10.5194/essd-13-4349-2021> (2021).
- 781 **83.** Cannon, A. J., Sobie, S. R. & Murdock, T. Q. Bias correction of GCM precipitation by quantile
782 mapping: How well do methods preserve changes in quantiles and extremes? *J. Clim.* **28**, 6938–6959,
783 <https://doi.org/10.1175/JCLI-D-14-00754.1> (2015).
- 784 **84.** Venema, V. K. C. *et al.* Benchmarking homogenization algorithms for monthly data. *Clim. Past* **8**,
785 89–115, <https://doi.org/10.5194/cp-8-89-2012> (2012).
- 786 **85.** Brönnimann, S. Climatic changes since 1700. In *Climatic Changes Since 1700*, 167–321, <https://doi.org/10.1007/978-3-319-19042-6> (Springer, 2015).
- 788 **86.** Domonkos, P., Guijarro, J. A., Venema, V., Brunet, M. & Sigró, J. Efficiency of Time Series
789 Homogenization: Method Comparison with 12 Monthly Temperature Test Datasets. *J. Clim.* **34**,
790 2877 – 2891, <https://doi.org/10.1175/JCLI-D-20-0611.1> (2021).
- 791 **87.** Gubler, S. *et al.* The influence of station density on climate data homogenization. *Int. J. Climatol.*
792 **37**, 4670–4683, <https://doi.org/10.1002/joc.5114> (2017).
- 793 **88.** Alexandersson, H. A homogeneity test applied to precipitation data. *J. Climatol.* **6**, 661–675,
794 <https://doi.org/10.1002/joc.3370060607> (1986).
- 795 **89.** Haimberger, L. Homogenization of Radiosonde Temperature Time Series Using Innovation Statistics.
796 *J. Clim.* **20**, 1377 – 1403, <https://doi.org/10.1175/JCLI4050.1> (01 Apr. 2007).
- 797 **90.** Menne, M. J. & Williams, C. N. Homogenization of temperature series via pairwise comparisons. *J.*
798 *Clim.* **22**, 1700–1717, <https://doi.org/10.1175/2008JCLI2263.1> (2009).
- 799 **91.** Browning, J. & Schneider, C. *snht: Standard Normal Homogeneity Test*, [https://CRAN.R-project.](https://CRAN.R-project.org/package=snht)
800 [org/package=snht](https://CRAN.R-project.org/package=snht) (2017). R package version 1.0.5.
- 801 **92.** Dunn, R. J. H., Willett, K. M., Morice, C. P. & Parker, D. E. Pairwise homogeneity assessment of
802 HadISD. *Clim. Past* **10**, 1501–1522, <https://doi.org/10.5194/cp-10-1501-2014> (2014).
- 803 **93.** Thorne, P. W. *et al.* Toward an integrated set of surface meteorological observations for climate
804 science and applications. *Bull. Am. Meteorol. Soc.* **98**, 2689 – 2702, [https://doi.org/10.1175/](https://doi.org/10.1175/BAMS-D-16-0165.1)
805 [BAMS-D-16-0165.1](https://doi.org/10.1175/BAMS-D-16-0165.1) (2017).
- 806 **94.** Brugnara, Y., Good, E., Squintu, A. A., van der Schrier, G. & Brönnimann, S. The EUSTACE global
807 land station daily air temperature dataset. *Geosci. Data J.* **6**, 189–204, <https://doi.org/10.1002/gdj3.81>
808 (2019).
- 809 **95.** Vincent, L. A., Zhang, X., Bonsal, B. R. & Hogg, W. D. Homogenization of Daily Temperatures over
810 Canada. *J. Clim.* **15**, 1322 – 1334, [https://doi.org/10.1175/1520-0442\(2002\)015<1322:HODTOC>2.](https://doi.org/10.1175/1520-0442(2002)015<1322:HODTOC>2.0.CO;2)
811 [0.CO;2](https://doi.org/10.1175/1520-0442(2002)015<1322:HODTOC>2.0.CO;2) (2002).
- 812 **96.** Jin, M. & Dickinson, R. E. Land surface skin temperature climatology: Benefitting from the
813 strengths of satellite observations. *Environ. Res. Lett.* **5**, 044004, [https://doi.org/10.1088/1748-9326/](https://doi.org/10.1088/1748-9326/5/4/044004)
814 [5/4/044004](https://doi.org/10.1088/1748-9326/5/4/044004) (2010).
- 815 **97.** Wan, Z., Hook, S. & Hulley, G. MODIS/Terra Land Surface Temperature/Emissivity 8-Day L3
816 Global 1km SIN Grid V006, <https://doi.org/10.5067/MODIS/MOD11A2.006> (2015).

- 817 **98.** Danielson, J. J. & Gesch, D. B. Global multi-resolution terrain elevation data 2010 (GMTED2010),
818 <https://doi.org/10.5066/F7J38R2N> (2011).
- 819 **99.** Holden, Z. A., Abatzoglou, J. T., Luce, C. H. & Baggett, L. S. Empirical downscaling of daily
820 minimum air temperature at very fine resolutions in complex terrain. *Agric. For. Meteorol.* **151**,
821 1066–1073, <https://doi.org/10.1016/j.agrformet.2011.03.011> (2011).
- 822 **100.** Gorelick, N. *et al.* Google Earth Engine: Planetary-scale geospatial analysis for everyone. *Remote.*
823 *sensing Environ.* **202**, 18–27, <https://doi.org/10.1016/j.rse.2017.06.031> (2017).
- 824 **101.** Aybar, C., Wu, Q., Bautista, L., Yali, R. & Barja, A. rgee: An R package for interacting with Google
825 Earth Engine. *J. Open Source Softw.* **5**, 2272, <https://doi.org/10.21105/joss.02272> (2020).
- 826 **102.** Parmentier, B. *et al.* Using multi-timescale methods and satellite-derived land surface temperature
827 for the interpolation of daily maximum air temperature in Oregon. *Int. J. Climatol.* **35**, 3862–3878,
828 <https://doi.org/10.1002/joc.4251> (2015).
- 829 **103.** Longman, R. J. *et al.* High-resolution gridded daily rainfall and temperature for the Hawaiian Islands
830 (1990–2014). *J. Hydrometeorol.* **20**, 489–508, <https://doi.org/10.1175/JHM-D-18-0112.1> (2019).
- 831 **104.** Newman, A. J. *et al.* Use of daily station observations to produce high-resolution gridded probabilistic
832 precipitation and temperature time series for the Hawaiian Islands. *J. Hydrometeorol.* **20**, 509–529,
833 <https://doi.org/10.1175/JHM-D-18-0113.1> (2019).
- 834 **105.** Newman, A. J., Clark, M. P., Wood, A. W. & Arnold, J. R. Probabilistic spatial meteorological
835 estimates for alaska and the yukon. *J. Geophys. Res. Atmospheres* **125**, e2020JD032696, <https://doi.org/10.1029/2020JD032696> (2020).
- 836 **106.** Hengl, T., Heuvelink, G. & Rossiter, D. About regression-kriging: from theory to interpretation of
837 results. *Comput. & Geosci.* **33**, 1301–1315, <https://doi.org/10.1016/j.cageo.2007.05.001> (2007).
- 838 **107.** Webster, R. & Oliver, M. A. Geostatistics for environmental scientists. *John Wiley & Sons*
839 <https://doi.org/10.1002/9780470517277> (2007).
- 840 **108.** Harris, P., Fotheringham, A., Crespo, R. & Charlton, M. The use of geographically weighted
841 regression for spatial prediction: an evaluation of models using simulated data sets. *Math. Geosci.*
842 **42**, 657–680, <https://doi.org/10.1007/s11004-010-9284-7> (2010).
- 843 **109.** Fotheringham, A. S., Brunson, C. & Charlton, M. Geographically weighted regression: the analysis
844 of spatially varying relationships. *John Wiley & Sons* (2003).
- 845 **110.** Gollini, I., Lu, B., Charlton, M., Brunson, C. & Harris, P. GWmodel: An R Package for Exploring
846 Spatial Heterogeneity Using Geographically Weighted Models. *J. Stat. Software, Articles* **63**, 1–50,
847 <https://doi.org/10.18637/jss.v063.i17> (2015).
- 848 **111.** Zhan, W. *et al.* Disaggregation of remotely sensed land surface temperature: Literature survey,
849 taxonomy, issues, and caveats. *Remote. Sens. Environ.* **131**, 119–139, <https://doi.org/10.1016/j.rse.2012.12.014> (2013).
- 850 **112.** Wang, S., Luo, X. & Peng, Y. Spatial Downscaling of MODIS Land Surface Temperature Based on
851 Geographically Weighted Autoregressive Model. *IEEE J. Sel. Top. Appl. Earth Obs. Remote. Sens.*
852 **13**, 2532–2546, <https://doi.org/10.1109/JSTARS.2020.2968809> (2020).
- 853 **113.** Zhang, X., Zwiers, F. W. & Hegerl, G. The influences of data precision on the calculation of
854 temperature percentile indices. *Int. J. Climatol.* **29**, 321–327, <https://doi.org/10.1002/joc.1738>
855 (2009).
- 856
857

- 858 **114.** Rhines, A., Tingley, M. P., McKinnon, K. A. & Huybers, P. Decoding the precision of historical
859 temperature observations. *Q. J. Royal Meteorol. Soc.* **141**, 2923–2933, [https://doi.org/10.1002/qj.](https://doi.org/10.1002/qj.2612)
860 [2612](https://doi.org/10.1002/qj.2612) (2015).
- 861 **115.** Pebesma, E. J. Multivariable geostatistics in S: the gstat package. *Comput. & geosciences* **30**,
862 683–691, <https://doi.org/10.1016/j.cageo.2004.03.012> (2004).
- 863 **116.** Gräler, B., Pebesma, E. & Heuvelink, G. Spatio-Temporal Interpolation using gstat. *The R Journal*
864 **8**, 204–218, <https://doi.org/10.32614/RJ-2016-014> (2016).
- 865 **117.** Hiemstra, P., Pebesma, E., Twenhöfel, C. & Heuvelink, G. Real-time automatic interpolation of
866 ambient gamma dose rates from the Dutch Radioactivity Monitoring Network. *Comput. Geosci.*
867 <http://dx.doi.org/10.1016/j.cageo.2008.10.011> (2008).
- 868 **118.** Huerta, A. *et al.* High-resolution grids of daily air temperature for Peru - the PISCOt v1.2 dataset,
869 <https://doi.org/10.6084/m9.figshare.c.5959863> (2022).
- 870 **119.** Willmott, C. J., Robeson, S. M. & Matsuura, K. A refined index of model performance. *Int. J.*
871 *Climatol.* **32**, 2088–2094, <https://doi.org/10.1002/joc.2419> (2012).
- 872 **120.** Legates, D. R. & McCabe, G. J. A refined index of model performance: a rejoinder. *Int. J. Climatol.*
873 **33**, 1053–1056, <https://doi.org/10.1002/joc.3487> (2013).
- 874 **121.** Lindeman, R. H. Introduction to bivariate and multivariate analysis. *Scott Foresman & Co* (1980).
- 875 **122.** Grömping, U. Relative importance for linear regression in R: the package relaimpo. *J. statistical*
876 *software* **17**, 1–27, <https://doi.org/10.18637/jss.v017.i01> (2007).
- 877 **123.** Dobrowski, S. Z., Abatzoglou, J. T., Greenberg, J. A. & Schladow, S. How much influence does
878 landscape-scale physiography have on air temperature in a mountain environment? *Agric. For.*
879 *Meteorol.* **149**, 1751–1758, <https://doi.org/10.1016/j.agrformet.2009.06.006> (2009).
- 880 **124.** Nichol, J. Remote sensing of urban heat islands by day and night. *Photogramm. engineering remote*
881 *sensing* **71**, 613–621, <https://doi.org/10.14358/PERS.71.5.613> (2005).
- 882 **125.** Moraes, A. G. d. L. *et al.* Terrain sensitive climate mapping for the Arequipa Department in Peru.
883 *Int. J. Climatol.* <https://doi.org/10.1002/joc.7730> (2022).
- 884 **126.** Zhang, M. *et al.* Creating new near-surface air temperature datasets to understand elevation-
885 dependent warming in the Tibetan Plateau. *Remote. Sens.* **12**, 1722, [https://doi.org/10.3390/](https://doi.org/10.3390/rs12111722)
886 [rs12111722](https://doi.org/10.3390/rs12111722) (2020).
- 887 **127.** Frei, C. Interpolation of temperature in a mountainous region using nonlinear profiles and non-
888 euclidean distances. *Int. J. Climatol.* **34**, 1585–1605, <https://doi.org/10.1002/joc.3786> (2014).
- 889 **128.** Abatzoglou, J. T., Dobrowski, S. Z., Parks, S. A. & Hegewisch, K. C. TerraClimate, a high-resolution
890 global dataset of monthly climate and climatic water balance from 1958-2015. *Sci. Data* **5**, 1–12,
891 <https://doi.org/10.1038/sdata.2017.191> (2018).
- 892 **129.** Bonshoms, M. *et al.* Validation of ERA5-Land temperature and relative humidity on four Peruvian
893 glaciers using on-glacier observations. *J. Mountain Sci.* **19**, 1849–1873, [https://doi.org/10.1007/](https://doi.org/10.1007/s11629-022-7388-4)
894 [s11629-022-7388-4](https://doi.org/10.1007/s11629-022-7388-4) (2022).
- 895 **130.** Pinche Laure, C. Estudio de las condiciones climáticas y de la niebla en la costa norte de Lima.
896 Tech. Rep., Universidad Nacional Agraria La Molina, Lima (Peru). Facultad de Ciencias (1986).
- 897 **131.** Schemenauer, R. S. & Cereceda, P. Meteorological conditions at a coastal fog collection site in Peru.
898 *Atmosfera* **6**, 175–188, <https://www.redalyc.org/articulo.oa?id=56506304> (1993).

- 899 **132.** Navarro-Serrano, F. *et al.* Maximum and minimum air temperature lapse rates in the Andean region
900 of Ecuador and Peru. *Int. J. Climatol.* **40**, 6150–6168, <https://doi.org/10.1002/joc.6574> (2020).
- 901 **133.** Walton, D. & Hall, A. An assessment of high-resolution gridded temperature datasets over California.
902 *J. Clim.* **31**, 3789–3810, <https://doi.org/10.1175/JCLI-D-17-0410.1> (2018).

903 **Acknowledgements**

904 The new version of PISCOt was developed with support by the Newton-Paulet fund within the project
905 'Water security and climate change adaptation in Peruvian glacier-fed river basins' (RAHU) under
906 the contract N°005-2019-FONDECYT. A.H. acknowledges additional financial support of the project
907 "Natural Infrastructure for Water Security" (NIWS), an initiative promoted and financed by the United
908 States Agency for International Development (USAID) and the Canadian Government. A.H. also ac-
909 knowledges financial support of the project 'Enhancing Adaptive Capacity of Andean Communities
910 through Climate Services' (ENANDES) executed by National Meteorological and Hydrological Ser-
911 vices of Colombia (IDEAM), Chile (DMC) and Peru (SENAMHI), and the WMO Regional Climate
912 Centre for Western South America (CIIFEN). P.R. acknowledges support from the fund KF400238
913 British Academy: El Niño and flash floods in Peru: Bringing knowledge on "Furia de los rios" and
914 "Western science" to understand lag time. We are grateful for the freely available global products:
915 ERA5-Land climate reanalysis data from the Copernicus Climate Change Service (C3S) Climate Data
916 Store at <https://cds.climate.copernicus.eu/>, the TerraClimate data from the Climatology Lab portal at
917 <https://www.climatologylab.org/terraclimate.html>; and, the CHIRTS data from the Climatic Hazard Center
918 at <https://www.chc.ucsb.edu/data>. In addition, PISCOt v1.1 was obtained from the IRI/LDEO Climate
919 Data Library at <http://iridl.ldeo.columbia.edu/SOURCES/.SENAMHI/.HSR/.PISCO/>; and VS2018 from
920 <http://hdl.handle.net/10261/139347>. We also are grateful for the freely available weather station dataset.
921 Due to the weather raw data used falling under the restriction of the policy of the South American
922 weather services, we can not share the entire raw database with this publication. Readers with an in-
923 terest in the raw data are asked to contact the respective weather services and institutions: SENAMHI
924 (<https://www.senamhi.gob.pe>) INAMHI (<https://www.inamhi.gob.ec>), IDEAM (<http://www.ideam.gov.co>),
925 INMET (<https://portal.inmet.gov.br>), and the Explorador Climático portal (<https://explorador.cr2.cl>).

926 **Author contributions statement**

927 A.H. led the publication, wrote the first draft of the manuscript, and developed the methodology in
928 consultation with W.L.C. A.H., C.A. and K.C. collected the station, reanalysis, and satellite data. A.H.
929 pre-processed the station data. A.H. and C.A. produced the gridding of station data. A.H. and N.I. validated
930 the data. O.F.B., P.R., F.D., and W.L.C. supervised the dataset construction and provided professional
931 advice. All authors were involved in discussions with regard to data development, and all reviewed the
932 manuscript.

933 **Competing interests**

934 The authors declare no competing interests.

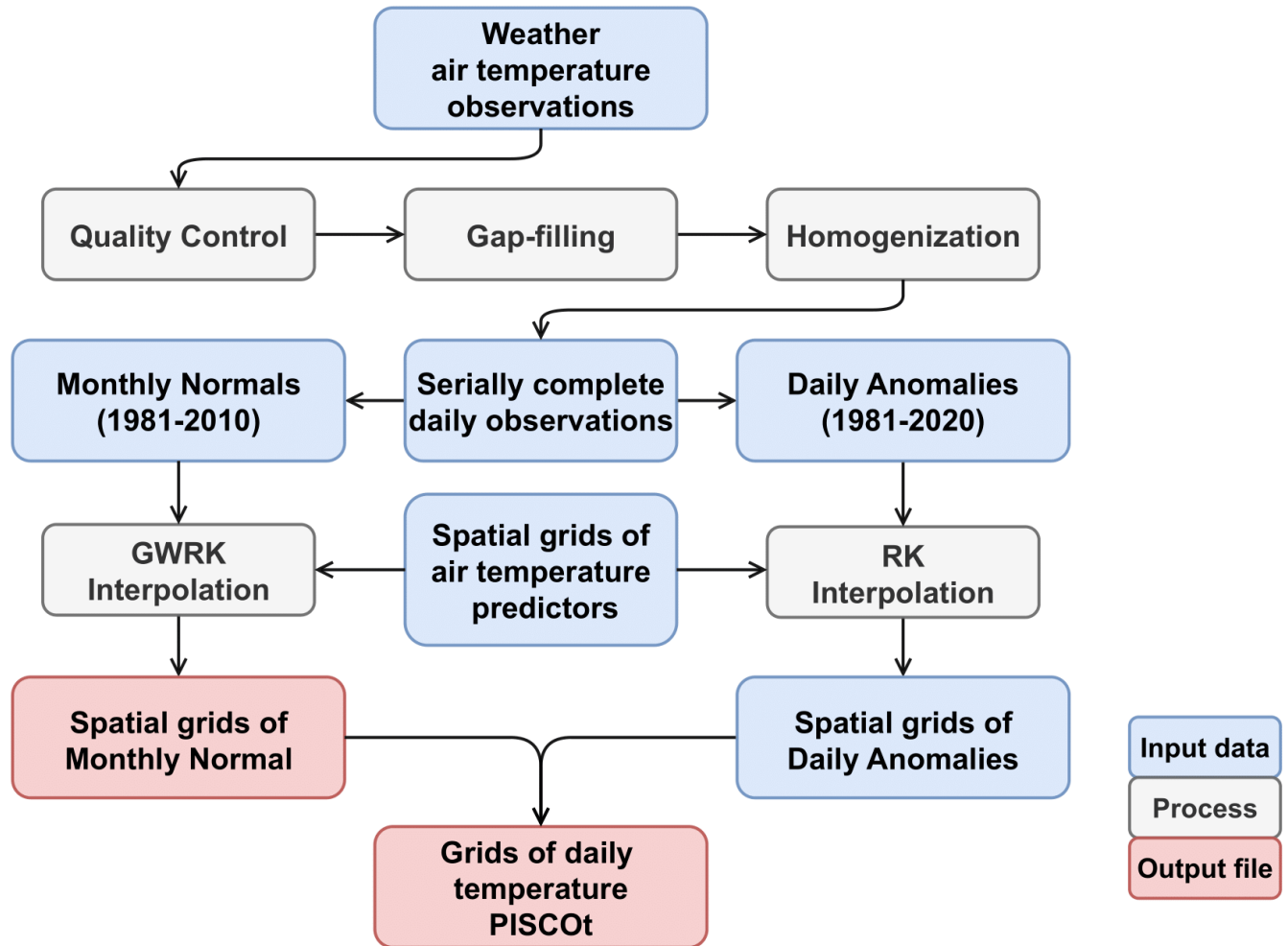


Figure 1. Schematic overview of the development of the daily air temperature gridded dataset (PISCOT). Input data, related processes, and main output files are specified. Spatial interpolation uses the Regression Kriging (RK) and Geographically Weighted Regression Kriging (GWRK) techniques.

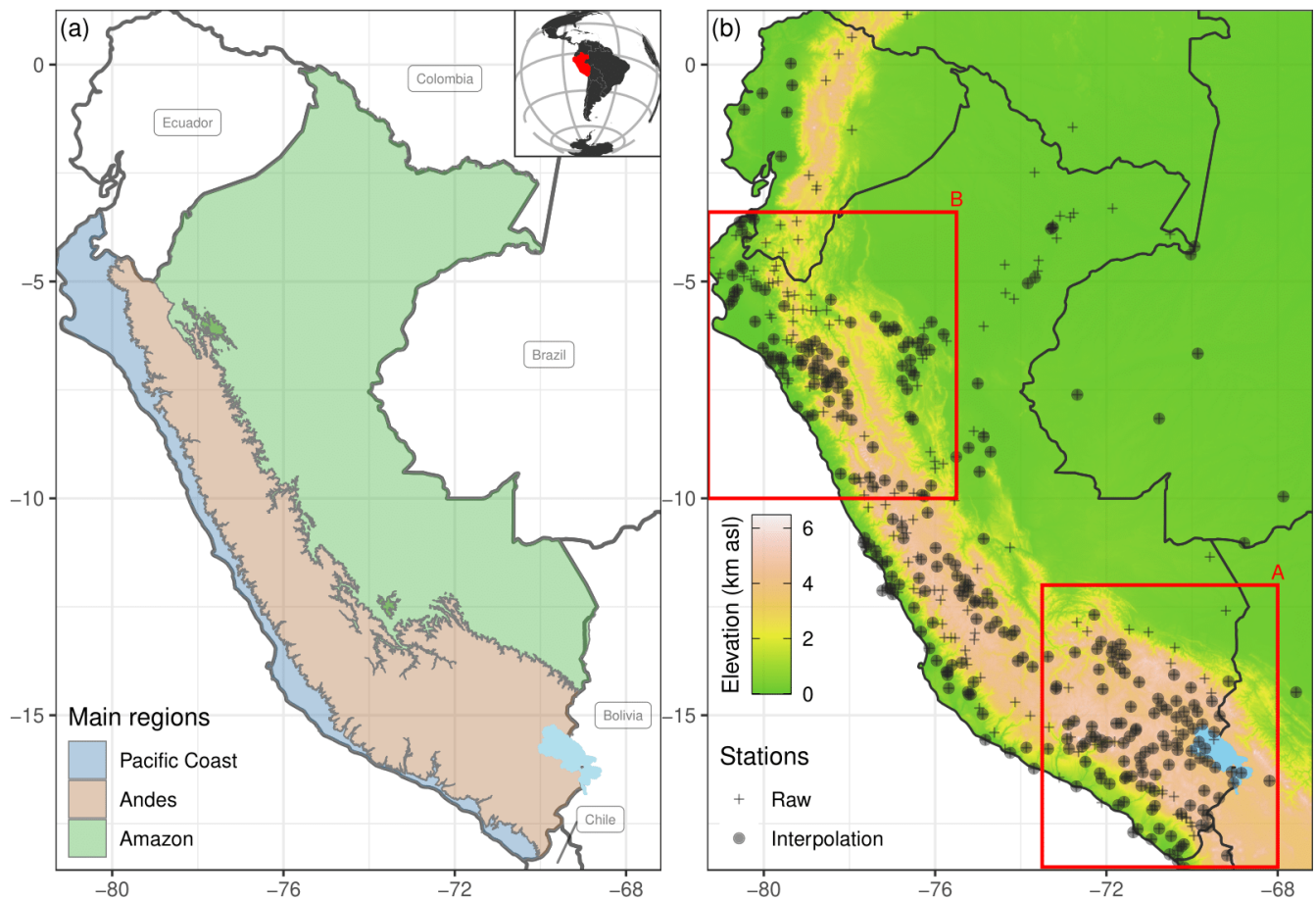


Figure 2. (a) Study area of Peru and its three main regions: Pacific Coast, Andes, and Amazon. The panel in the upper right corner shows the location of the study area in South America. (b) Spatial distribution of 462 available time series (Raw) for daily maximum (Tmax) and minimum (Tmin) temperature. After the data pre-processing, 302 time series were used for spatial interpolation (Interpolation). The red boxes represent the southern (A) and northern (B) Andes areas of Peru. Lake Titicaca is shown in light blue.

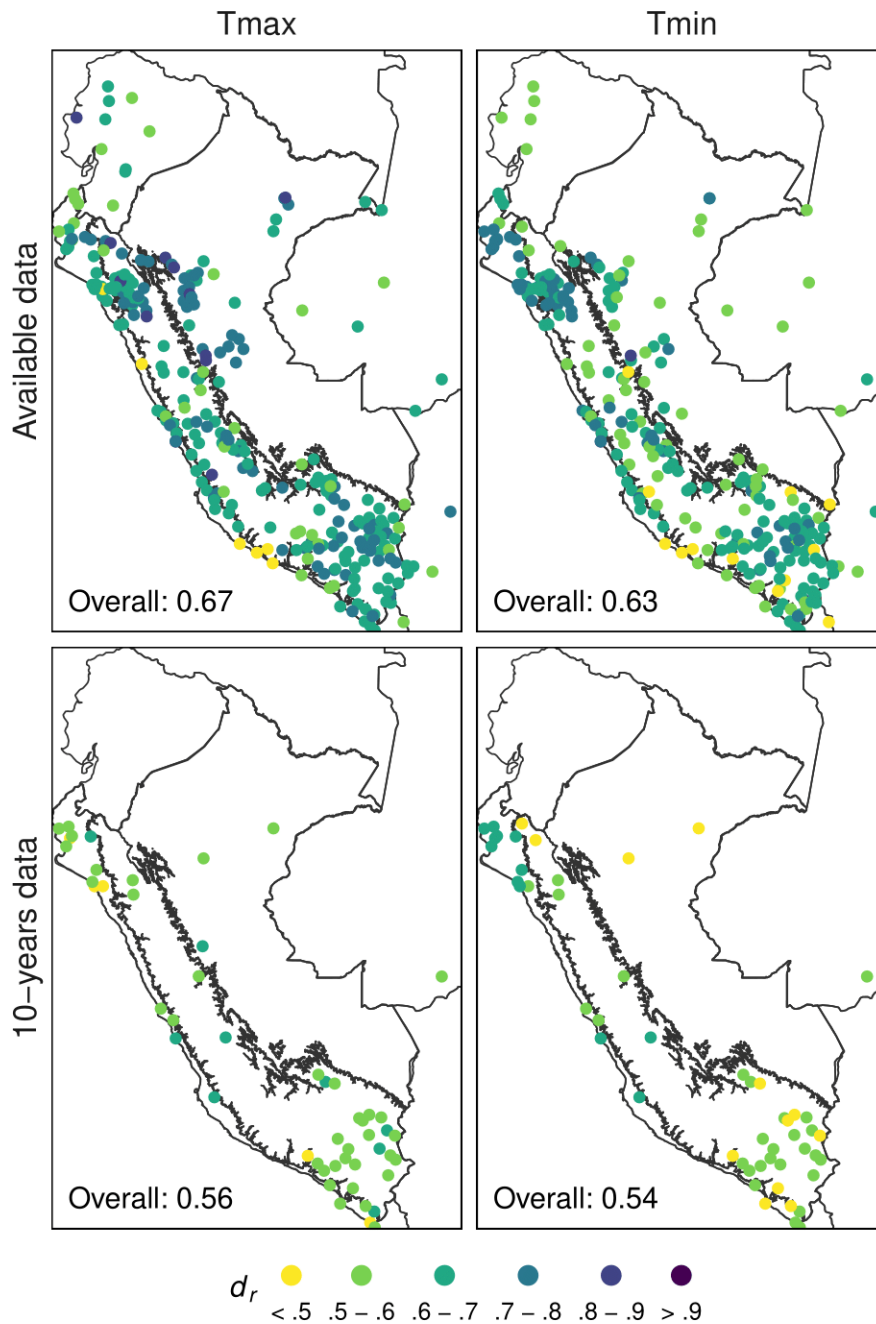


Figure 3. Spatial distribution of the refined index of agreement (d_r) for gap filling (1981-2020) of daily maximum (Tmax) and minimum (Tmin) air temperature in two experiments: validation, using all available data; and, cross-validation, when only a complete period of 10-years (with $\geq 75\%$ data) is available. Black lines represent the three main climate regions: Pacific Coast (Western Peru), Andes (Central Peru), and Amazon (Eastern Peru).

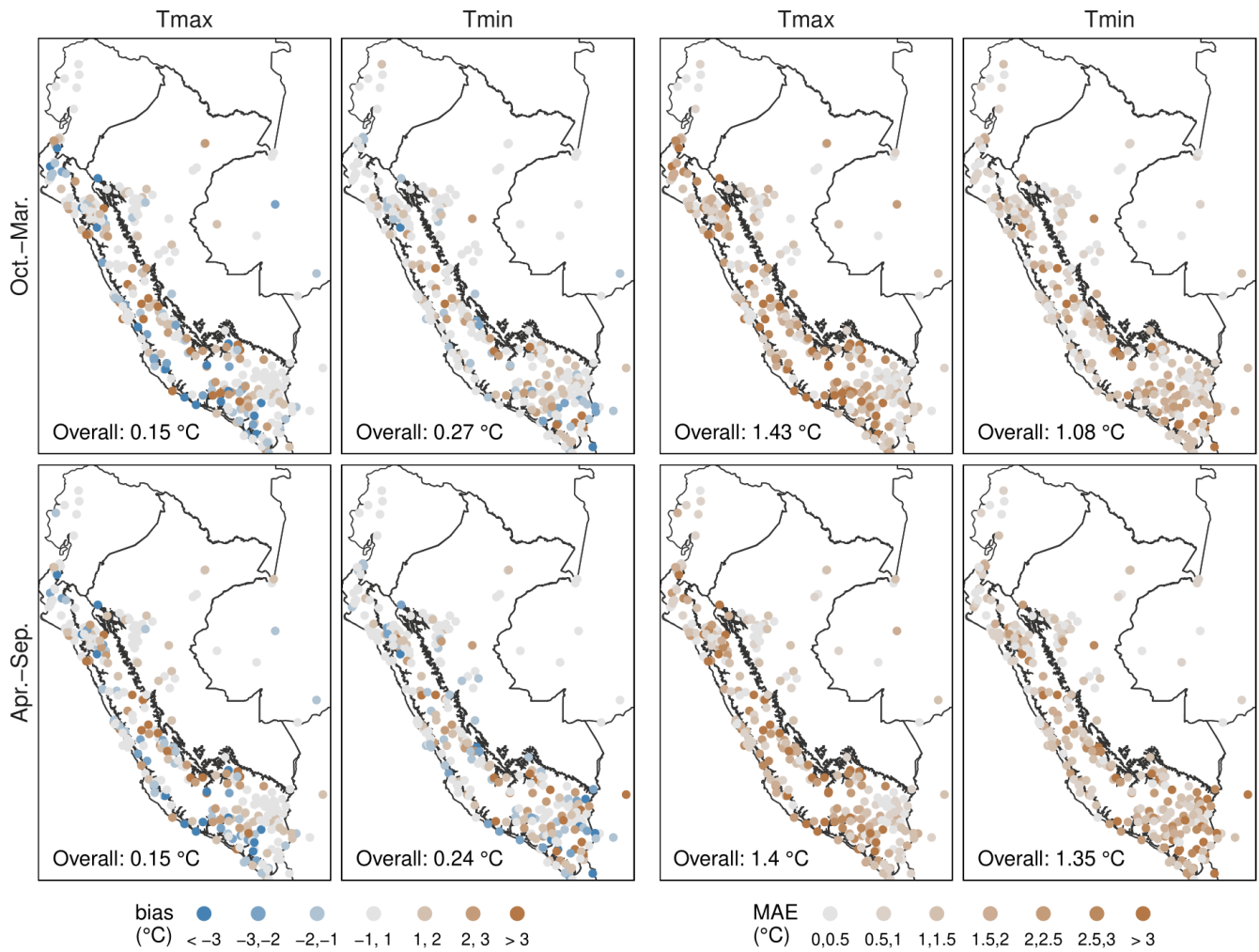


Figure 4. 10-fold cross-validation bias and mean absolute error (MAE) for interpolated monthly maximum (Tmax) and minimum (Tmin) normal temperature in the period 1981-2010 ($n = 299$ stations). Black lines represent the three main climate regions in Peru (Fig. 3)

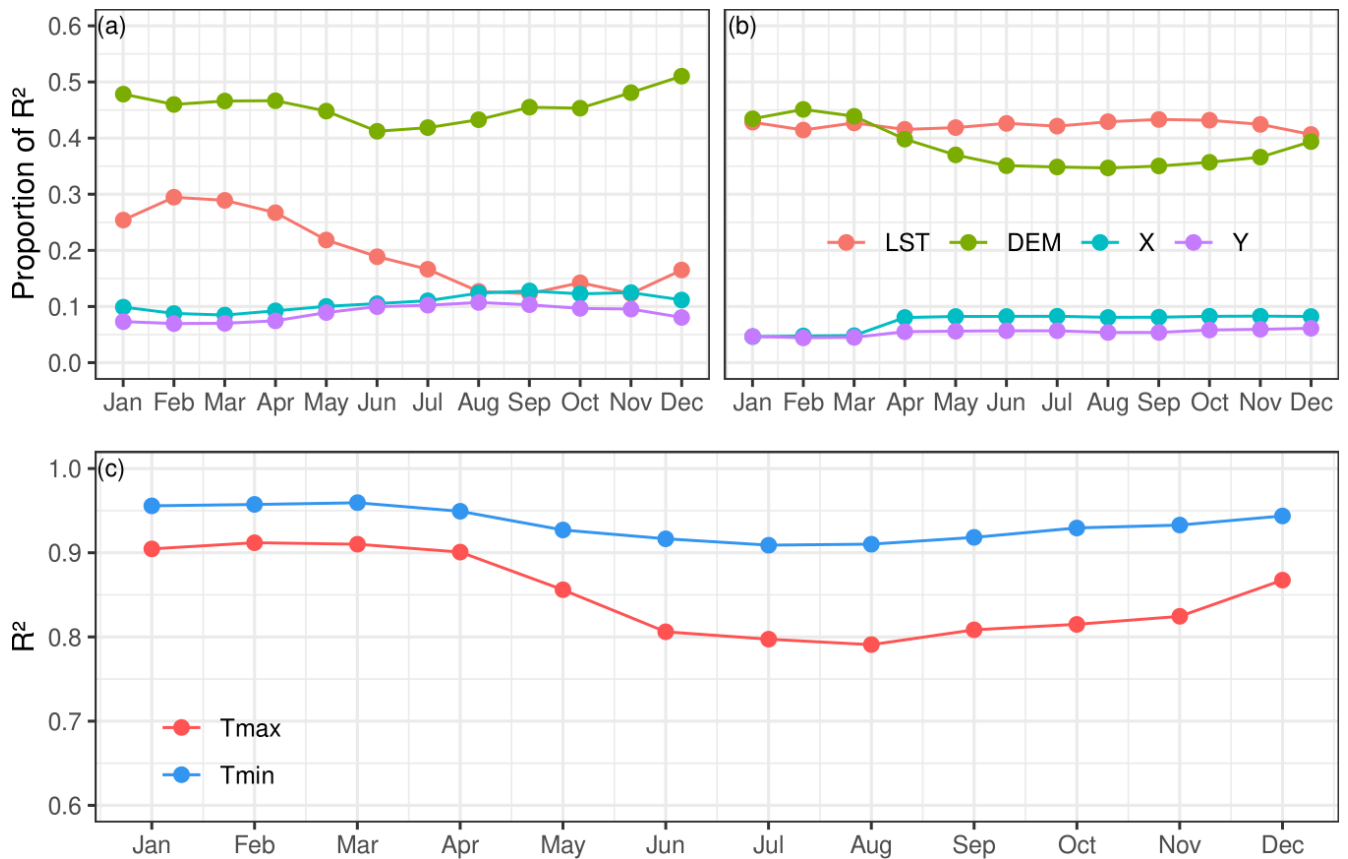


Figure 5. Relative and absolute influence of spatial predictors (land surface temperature (LST), elevation (DEM), latitude (Y), and longitude (X)) over Peru using a monthly-normal moving window with multiple linear regression relating the Geographically Weighted Regression Kriging (GWRK). Proportion of variance explained (R^2) of each predictor for (a) maximum air temperature (Tmax) and (b) minimum air temperature (Tmin); and, (c) overall R^2 . The statistical values are averaged over 253 stations.

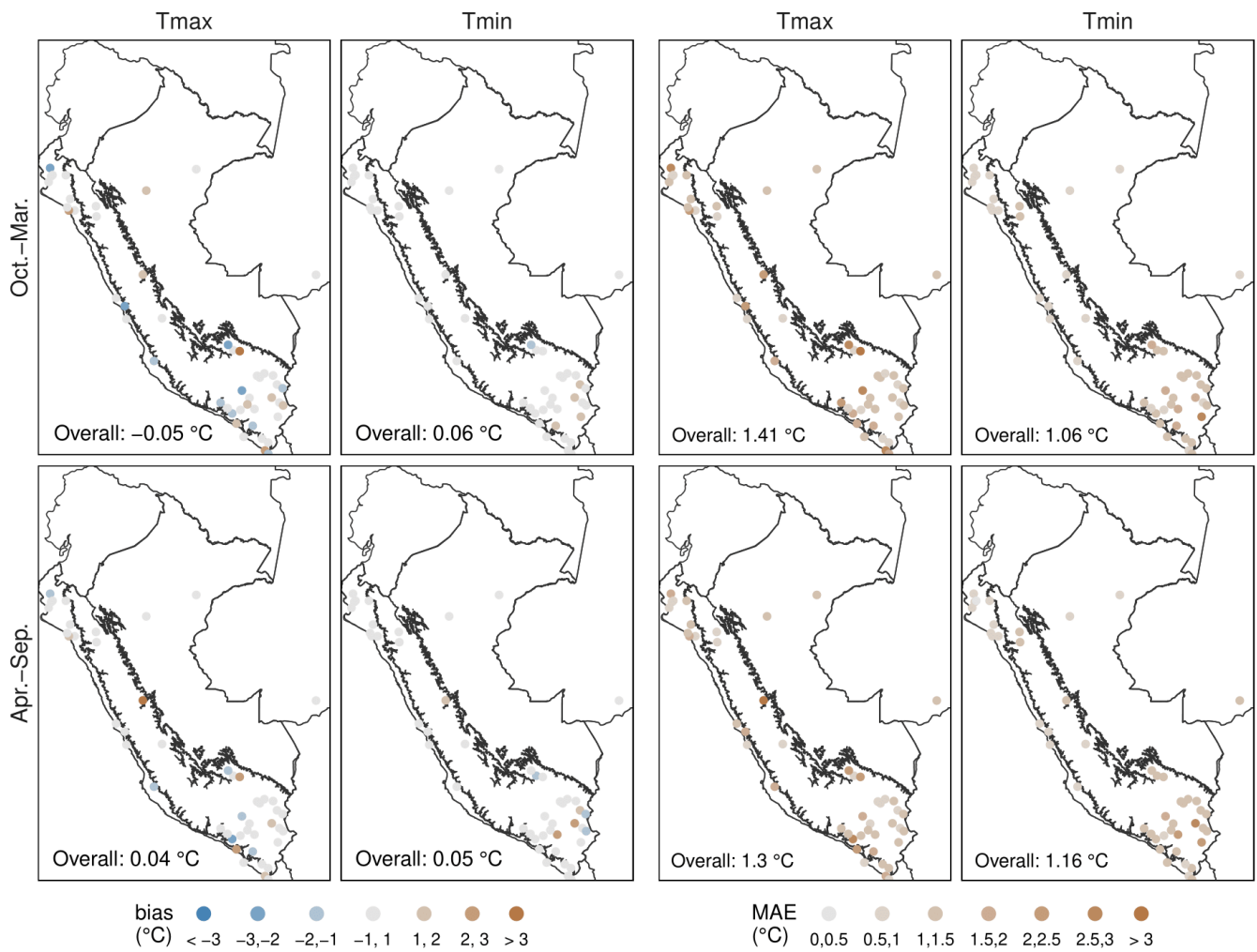


Figure 6. 10-fold cross-validation bias and mean absolute error (MAE) for interpolated daily maximum (Tmax) and minimum (Tmin) temperature in the period 1981-2010 ($n = 48$ stations). Black lines represent the three main climate regions in Peru (Fig. 3)

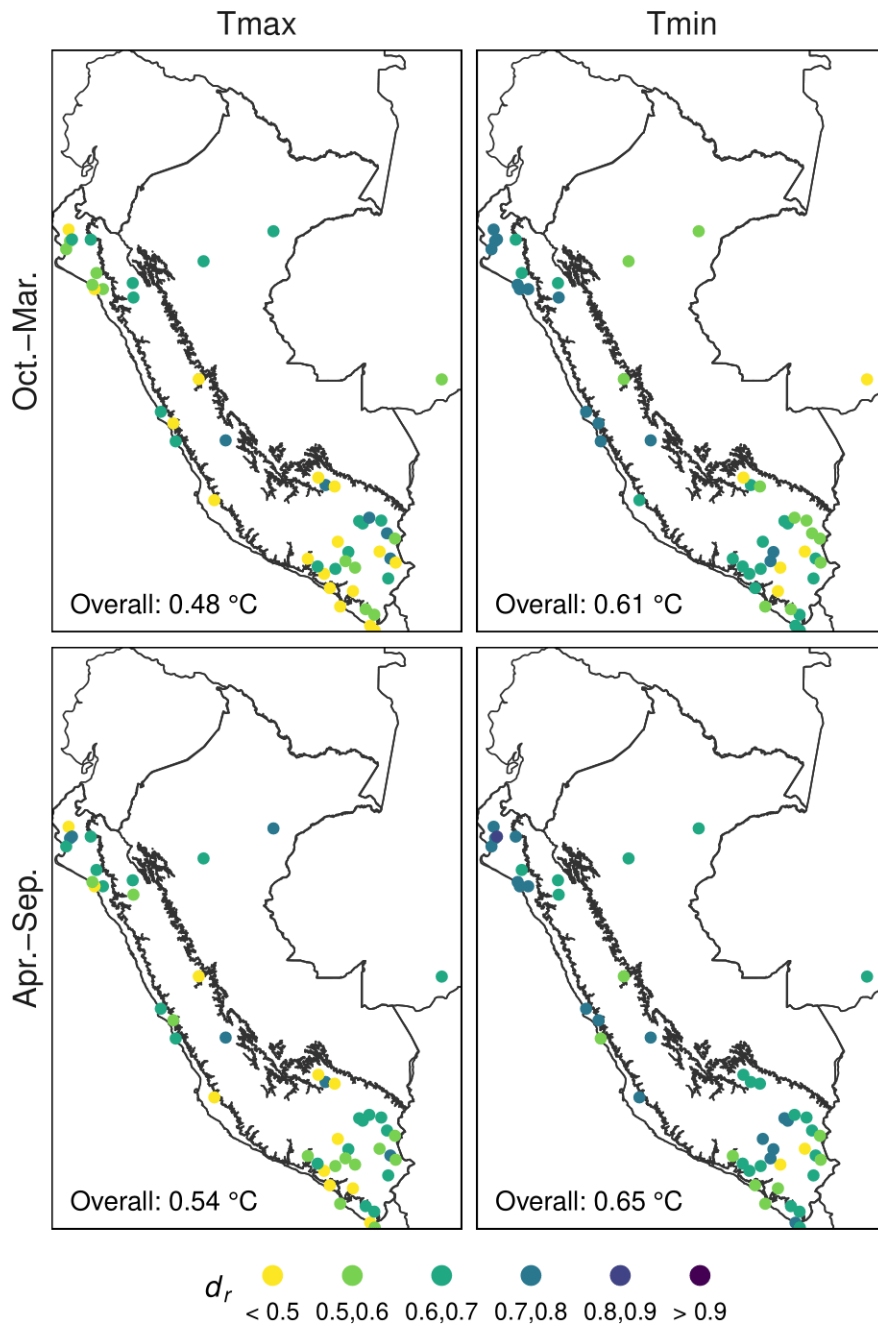


Figure 7. 10-fold cross-validation refined index of agreement (d_r) for interpolated daily maximum (Tmax) and minimum (Tmin) temperature in the period 1981-2010 ($n = 48$ stations). Black lines represent the three main climate regions in Peru (Fig. 3).

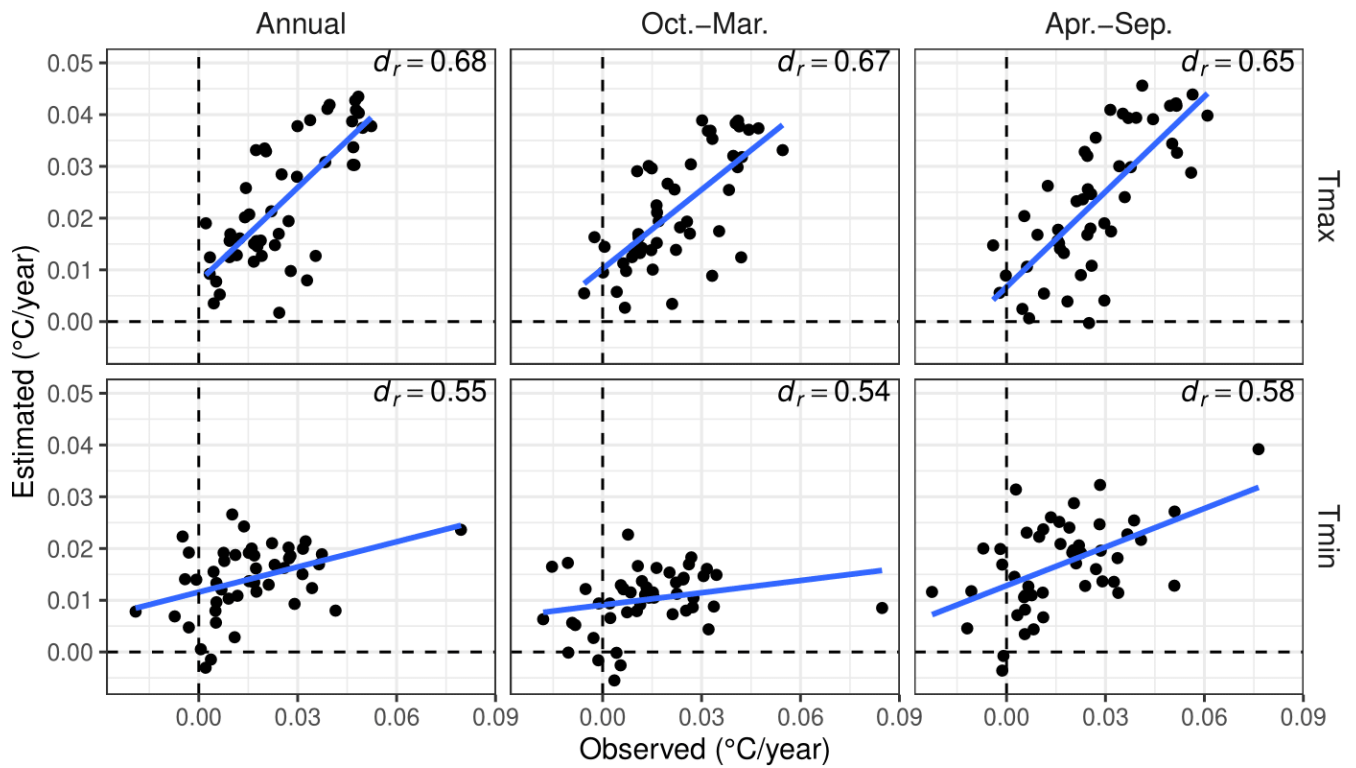


Figure 8. Scatterplot of estimated (10-fold cross-validation) and observed air maximum (Tmax) and minimum (Tmin) temperature trends (Sen’s slope) in the period 1981-2020. Mean values at annual; and October-March and April-September mean seasons. Blue lines (linear regression) show the agreement between observed and estimated trends. The refined index of agreement (d_r) is also shown for each plot ($n = 48$ stations).

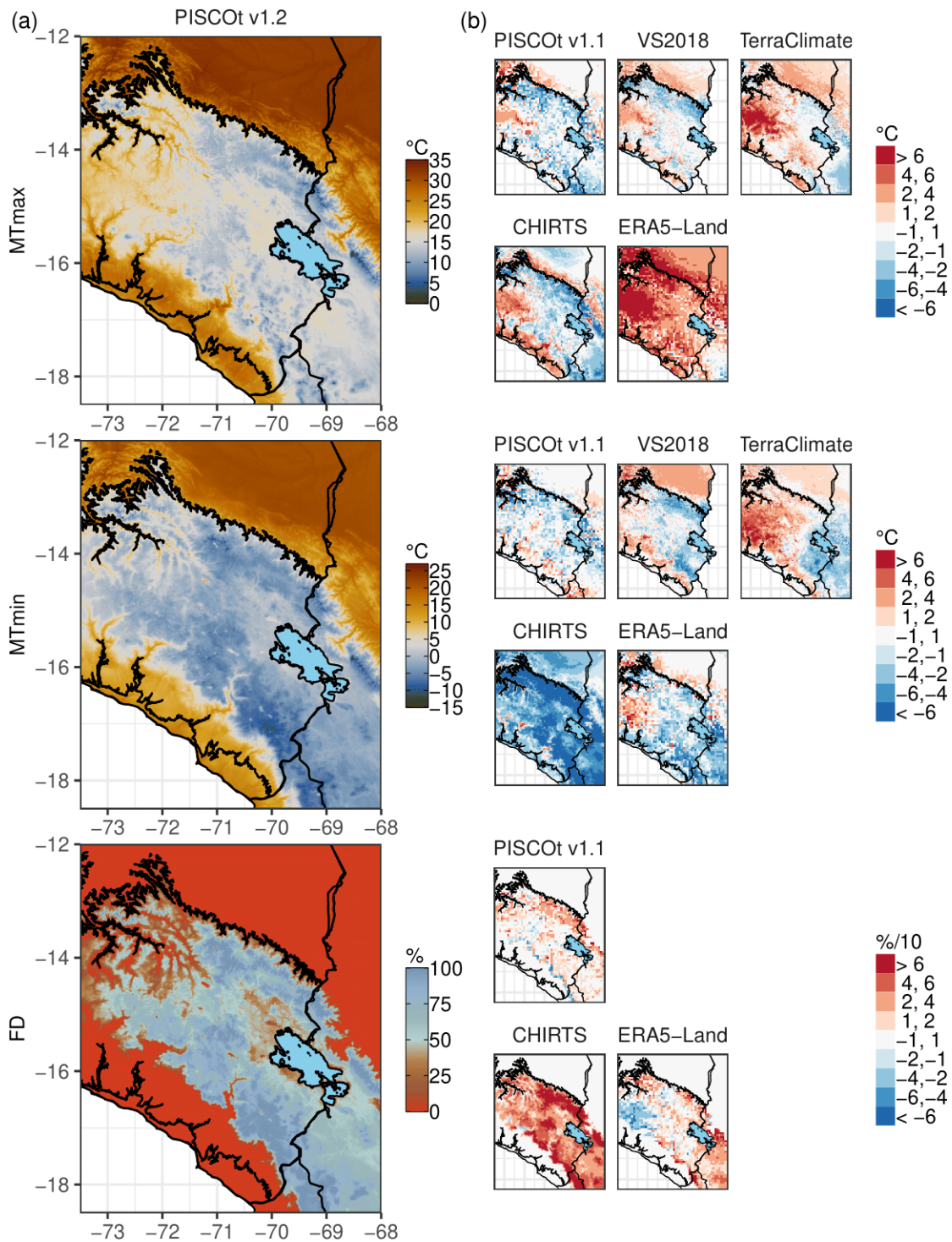


Figure 9. Spatial distribution and differences of the mean annual (1981-2010) temperature indices (mean Tmax (MTmax), mean Tmin (MTmin), and frost days (FD)) in the southern Andes of Peru. (a) Spatial distribution for PISCOT v1.2. (b) Difference of PISCOT v1.2 with each gridded product (PISCOT v1.1, VS2018, TerraClimate, CHIRTS, and ERA5-Land) and temperature indices. For CHIRTS, the mean average corresponds to 1983-2010. Black lines represent the three main climate regions in Peru (Fig. 3); Lake Titicaca is shown as a lightblue filled area.

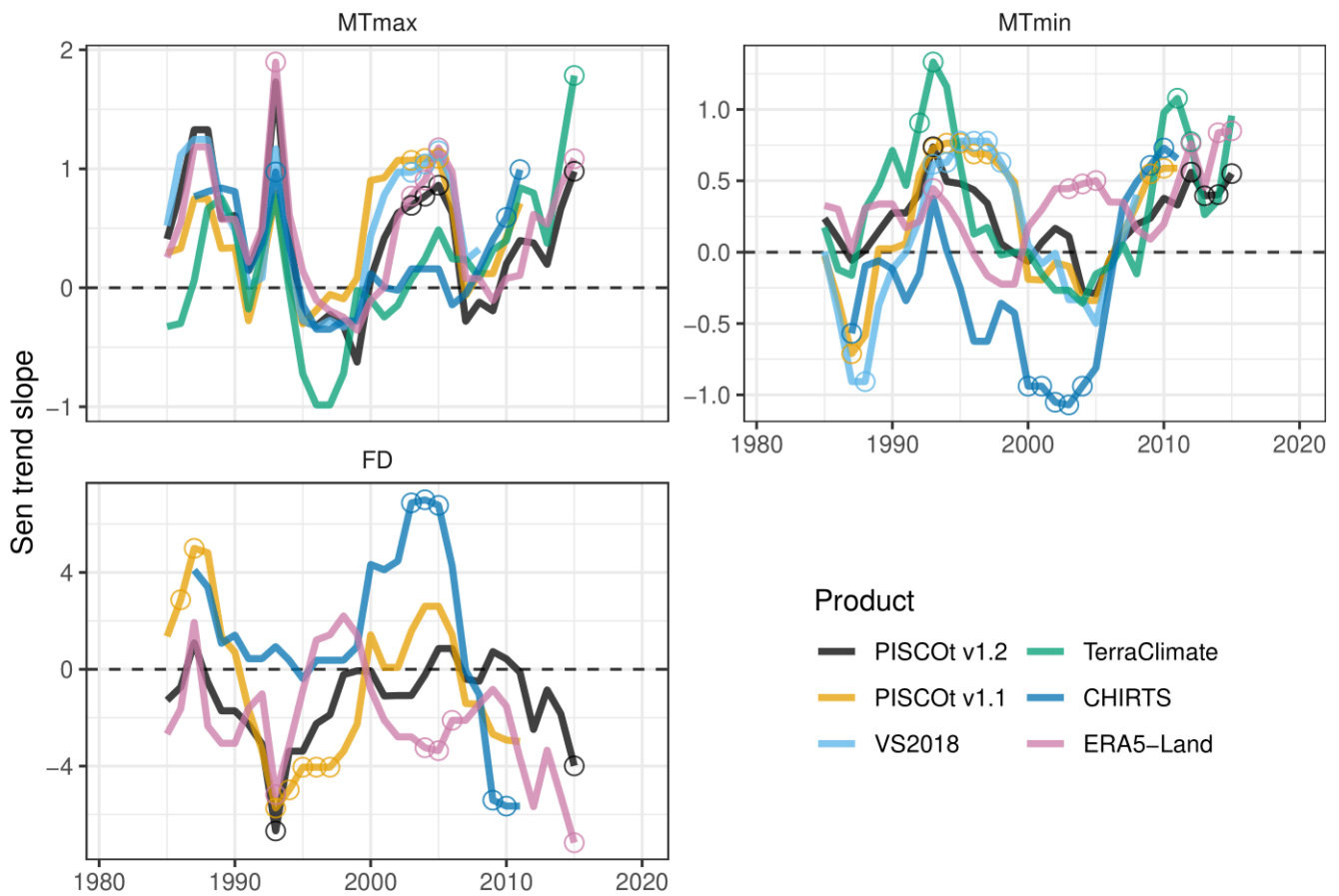


Figure 10. Running annual Sen’s slope (for 10-years window from 1981 to 2020) of temperature indices (mean Tmax (MTmax), mean Tmin (MTmin), and frost days (FD)) for PISCOt v1.2 and gridded products (PISCOt v1.1, VS2018, TerraClimate, CHIRTS, and ERA5-Land) in the southern Andes of Peru (following delimitation of red box in Fig. 2 considering all land > 2000 masl). Significant trend estimates (Mann–Kendall trend test with $p < 0.05$) are shown with an open circle. The x-axis shows the centroid year of running trends.

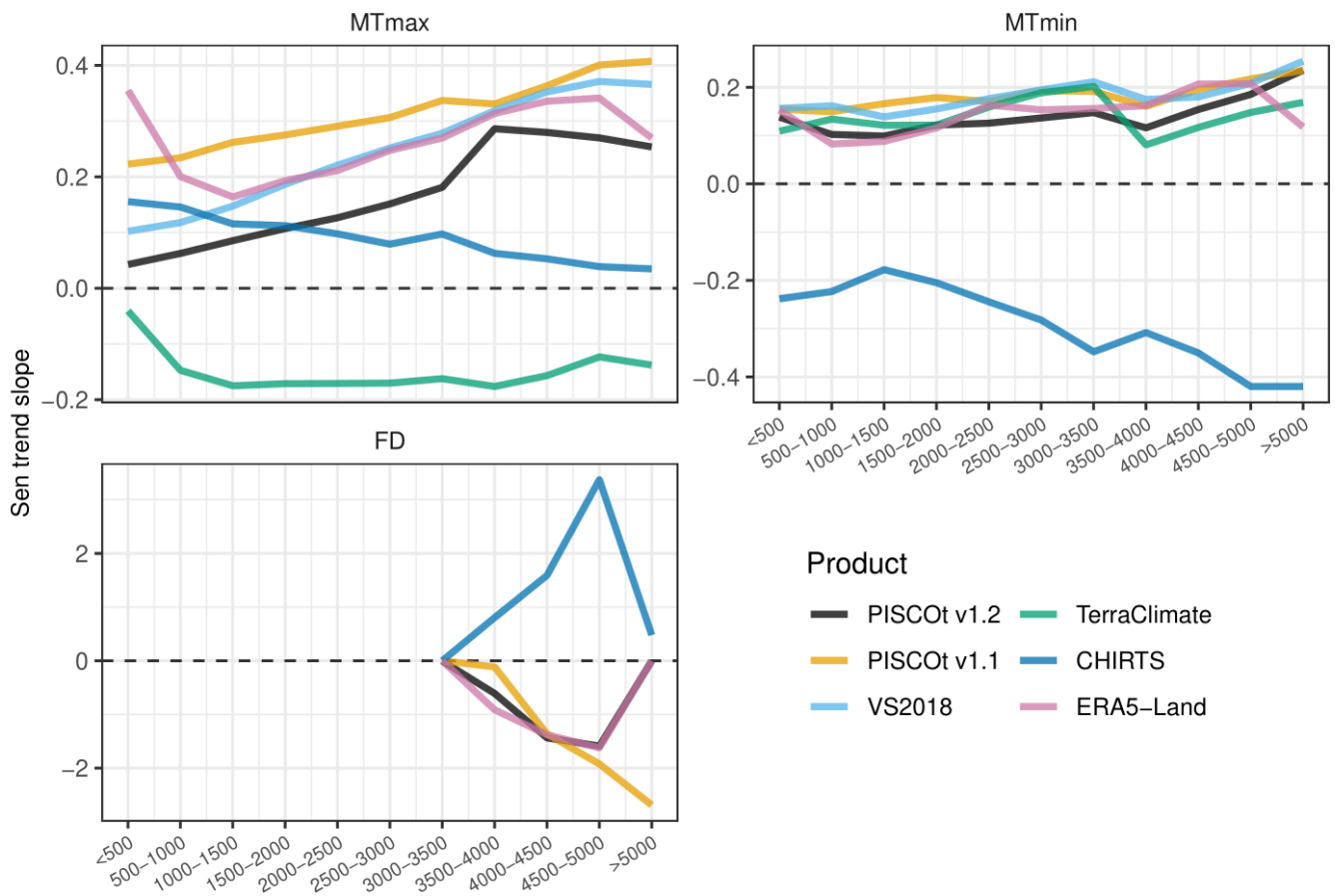


Figure 11. Annual Sen's slope (1983-2013) of temperature indices (mean Tmax (MTmax), mean Tmin (MTmin), and frost days (FD)) per different elevations intervals (km asl.) for PISCOT v1.2 and gridded products (PISCOT v1.1, VS2018, TerraClimate, CHIRTS, and ERA5-Land) over the southern Andes of Peru.

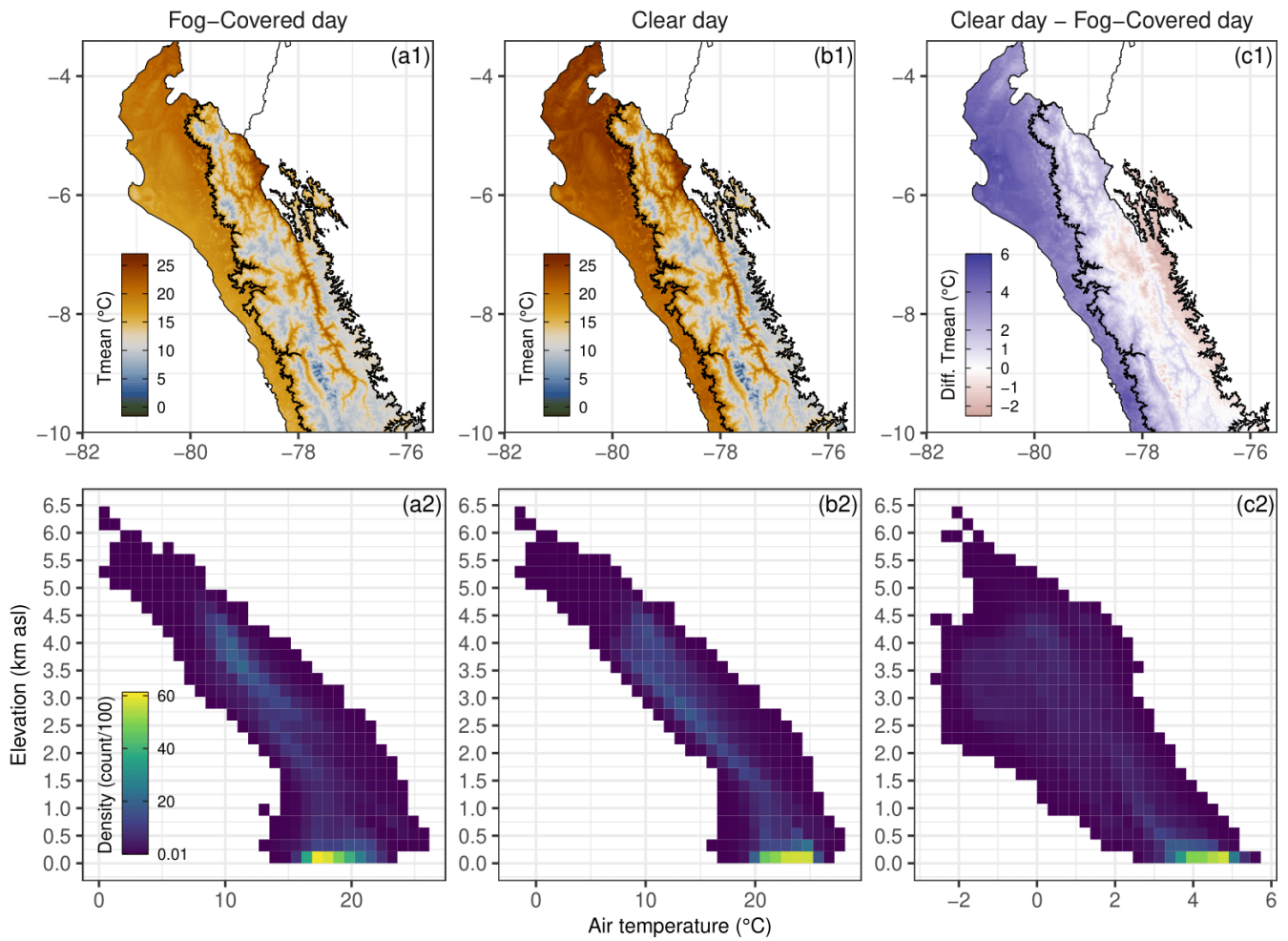


Figure 12. Examples of mean air temperature (Tmean: mean Tmax and Tmin) in two conditions of coastal fog-covered (a1; Fog-Covered day) and cloud-free (a2; Clear day) day for northern regions (Pacific Coast and Andes) of Peru. In addition, the difference between the Tmean of both days is shown (a3; Clear-day - Fog-Covered day). The vertical distribution of Tmean is also represented in lower panels as scatterplots of 2D bin counts (b1, b2, and b3, respectively). Black lines represent the three main climate regions in Peru (Fig. 3).

Order	Repository Name	Data	Format	Number of files	Files	Access
1	Maximum temperature (PISCOt v1.2)	Tmax	.nc	41	tmax_mean_1981-2010.nc, tmax_daily_1981.nc, ⋮ tmax_daily_2020.nc	https://doi.org/10.6084/m9.figshare.20522806
2	Minimum temperature (PISCOt v1.2)	Tmin	.nc	41	tmin_mean_1981-2010.nc, tmin_daily_1981.nc, ⋮ tmin_daily_2020.nc	https://doi.org/10.6084/m9.figshare.20533715
3	Spatial Covariables for PISCOt v1.2	DEM, Y, X, TDI, LST_day, LST_night	.nc	6	DEM.nc, Y.nc, X.nc, TDI.nc, LST_day.nc, LST_night.nc	https://doi.org/10.6084/m9.figshare.15167517
4	Weather stations used in PISCOt v1.2	list of weather stations	.csv	1	xyz_qc_gf_hmg.csv	https://doi.org/10.6084/m9.figshare.14329208
5	Maximum and Minimum temperature at a coarser resolution (PISCOt v1.2)	Tmax, Tmin	.nc	8	tmax_mean_1981-2010_005.nc, tmin_mean_1981-2010_005.nc, tmax_daily_1981_2020_005.nc, tmin_daily_1981_2020_005.nc, tmax_mean_1981-2010_010.nc, tmin_mean_1981-2010_010.nc, tmax_daily_1981_2020_010.nc, tmin_daily_1981_2020_010.nc	https://doi.org/10.6084/m9.figshare.22712365

Table 1. Accession and data files for each repository of the database.

Experiment	Tmax				Tmin			
	Number of stations	bias (°C)	MAE (°C)	d_r	Number of stations	bias (°C)	MAE (°C)	d_r
Validation (Available data)	346	0.11	0.98	0.67	342	0.1	0.98	0.63
Cross-validation (10-years data)	51	0.03	1.27	0.56	52	-0.02	1.44	0.54

Table 2. Gap filling error statistics for daily maximum (Tmax) and minimum (Tmin) temperature for bias, mean absolute error (MAE), and refined index of agreement (d_r) for 1981-2020 in two experiments: using all available data and when only a complete period of 10-years (with $\geq 75\%$ data) is available.